Journal of Colloid and Interface Science 513 (2018) 515–526

Contents lists available at ScienceDirect

Journal of Colloid and Interface Science

journal homepage: www.elsevier.com/locate/jcis

Regular Article

Rheology of particle/water/oil three-phase dispersions: Electrostatic vs. capillary bridge forces

Mihail T. Georgiev [a], Krassimir D. Danov [a], Peter A. Kralchevsky [a,*], Theodor D. Gurkov [a], Denitsa P. Krusteva [a], Luben N. Arnaudov [b], Simeon D. Stoyanov [b,c,d], Eddie G. Pelan [b]

[a] Department of Chemical & Pharmaceutical Engineering, Faculty of Chemistry and Pharmacy, Sofia University, Sofia 1164, Bulgaria
[b] Unilever Research & Development Vlaardingen, 3133AT Vlaardingen, The Netherlands
[c] Laboratory of Physical Chemistry and Colloid Science, Wageningen University, 6703 HB Wageningen, The Netherlands
[d] Department of Mechanical Engineering, University College London, WC1E 7JE, UK

GRAPHICAL ABSTRACT

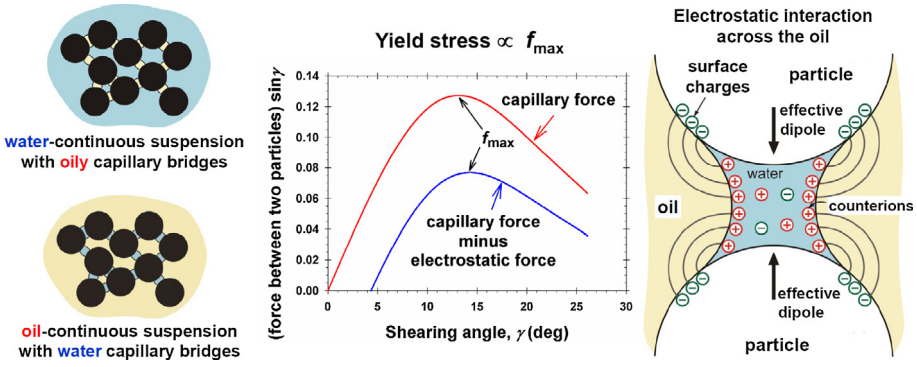

ARTICLE INFO

Article history:
Received 14 October 2017
Revised 16 November 2017
Accepted 17 November 2017
Available online 22 November 2017

Keywords:
Capillary bridges
Silica particles
Capillary suspensions
Pendular state
Yield stress
Suspension rheology
Wet granular materials

ABSTRACT

Hypothesis: Particle/water/oil three-phase capillary suspensions possess the remarkable property to solidify upon the addition of minimal amount of the second (dispersed) liquid. The hardening of these suspensions is due to capillary bridges, which interconnect the particles (pendular state). Electrostatic repulsion across the oily phase, where Debye screening by electrolyte is missing, could also influence the hardness of these suspensions.

Experiments: We present data for oil-continuous suspensions with aqueous capillary bridges between hydrophilic SiO_2 particles at particle volume fractions 35–45%. The hardness is characterized by the yield stress Y for two different oils: mineral (hexadecane) and vegetable (soybean oil).

Findings and modelling: The comparison of data for the "mirror" systems of water- and oil-continuous capillary suspensions shows that Y is lower for the oil-continuous ones. The theoretical model of yield stress is upgraded by including a contribution from electrostatic repulsion, which partially counterbalances the capillary-bridge attraction and renders the suspensions softer. The particle charge density determined from data fits is close to that obtained in experiments with monolayers from charged colloid particles at oil/water interfaces. The results could contribute for better understanding, quantitative prediction and control of the mechanical properties of solid/liquid/liquid capillary suspensions.

* Corresponding author at: Sofia University, Faculty of Chemistry and Pharmacy, James Bourchier Blvd. No. 1, Sofia 1164, Bulgaria.
E-mail address: pk@lcpe.uni-sofia.bg (P.A. Kralchevsky).

https://doi.org/10.1016/j.jcis.2017.11.057
0021-9797/

1. Introduction

Here, we investigate three-phase suspensions, in which solid colloid particles are dispersed together with two immiscible liquids, water and oil (liquid hydrocarbon). One of the two liquids serves as continuous phase. A remarkable property of such suspensions is that the addition of even minimal amounts of the second (dispersed) liquid, called the *inner liquid*, leads to hardening of dispersion [1–6]. Hardening may happen in the cases of both acute and obtuse three-phase contact angles, α. In the former case ($\alpha < 90°$), the inner liquid forms *capillary bridges* (pendular rings) [7,8] that interconnect the solid particles. The respective dispersion morphology is known as the *pendular state*. In the latter case ($\alpha > 90°$), the capillary bridges are unstable [9], but the inner liquid fills the gaps between the particles, which are interconnected by the formed oil/water *capillary menisci*; the respective morphology is known as the *capillary state* of dispersion [1–4]. At comparable volume fractions of the two liquids, dispersion with two bicontinuous liquid phases, termed *bijel*, could be formed [10–13].

These three-phase dispersions, called *capillary suspensions*, could find various applications, such as the preparation of novel food products [14,15]; slurries for printable electronics or generation of energy [16–19]; improved polymer blends [20–22]; precursors for glass or ceramic filters of high porosity [23–25], and thermal interfacial materials [26]. Additional information could be found in recent review articles [4,6,27].

Our study is focused on the mechanical properties of capillary suspensions in the *pendular* state, in which the particles are interconnected by capillary bridges. Such suspensions could be *water-continuous*, if hydrophobic particles are dispersed in water together with small amounts of oil, which forms capillary bridges (Fig. 1a). In the "mirror" system (Fig. 1b), the dispersion is *oil-continuous*; the particles are hydrophilic and the inner liquid is water. The saturation of the dispersion with the inner liquid can be characterized by the relative volume fraction of this liquid with respect to the total volume of the liquid phases:

$$S_i = \frac{\phi_i}{\phi_w + \phi_{oil}}, \ i = \ w, \ oil \tag{1}$$

Here, ϕ_w and ϕ_{oil} are, respectively, the volume fractions of water and oil in the dispersion; $\phi_w + \phi_{oil} + \phi_p = 1$, where ϕ_p is the volume fraction of particles in the dispersion. For capillary suspensions in the pendular state, the content of inner liquid is usually in the range $0.001 \leq S_i \leq 0.1$. What concerns the particle volume fraction, ϕ_p, *uniform* suspensions from monodisperse spherical particles (without voids comparable with, or larger than, the particle size) can be formed for $0.34 \leq \phi_p \leq 0.74$ [27]. The upper limit, $\phi_p = 0.74$, corresponds to close packing of colloidal spheres with $n = 12$ pendular rings formed in the contact zones of the neighboring particles. The lower limit, $\phi_p = 0.34$, corresponds to the lattice structure of diamond with $n = 4$ closest neighbors and four capillary bridges per particle. In capillary suspensions, the mean number of capillary bridges per particle (the coordination number), n, can vary continuously with the rise of the particle volume fraction, ϕ_p. A simple relation for estimation of n was obtained [27]:

$$n \approx 11.67\phi_p \text{ for } \phi_p \leqslant 0.68 \tag{2}$$

It should be noted that hardening of capillary suspensions can be observed also for $\phi_p < 0.34$. In this case, particles interconnected by capillary menisci may form networks (with big voids) that span the whole space occupied by the dispersion [4,28].

If a capillary suspension is subjected to shear stress, it initially undergoes a quasi-elastic deformation, followed by a transition to viscoelastic flow. This transition happens at the elastic limit characterized by the yield stress, Y. It was demonstrated that the projection of the capillary-bridge force on the shear plane has a maximal value. The capillary bridge cannot withstand an applied external force that exceeds this maximal value, which is related to the elastic limit and the yield stress. The following expression for the yield stress, Y, was obtained [27]:

$$Y = \frac{2\sigma}{a} c_g \phi_p^{2/3} f_{cap,max}(\Phi, \alpha) \tag{3}$$

Y increases with the rise of the interfacial tension, σ, and with the decrease of the particle radius, a; the term $c_g\phi_p^{2/3}$ is proportional to the number of bridges per unit area of the shear plane; the geometrical coefficient c_g may depend not only on geometrical factors, but also on dynamic factors related to the bridge formation during the stirring/preparation of the suspension; Φ is the volume of the capillary bridge scaled with the volumes of the two adjacent particles; α is the three-phase contact angle measured across the bridge phase; $f_{cap,max}(\Phi,\alpha)$ is a dimensionless universal function that has been computed using the exact theory of capillary bridges and tabulated in Ref. [27]. Therein, for fast estimates of $f_{cap,max}(\Phi,\alpha)$ an approximate equation (of accuracy better than 0.6%) was obtained:

$$f_{cap,max}(\Phi, \alpha) \approx (0.1763 + 0.0912\phi + 0.0165\phi^2)\cos\alpha \text{ for } \alpha \leqslant \alpha_0$$
$$\alpha_0(\text{deg}) = 51.5 - 19.5\varphi - 2.5\varphi^2, \ \varphi = \log_{10}\Phi(\%) \tag{4}$$

$0.01\% \leq \Phi \leq 10\%$; see Appendix B for details. Φ is related to S_i by the relation

$$S_i = \frac{n\Phi}{1/\phi_p - 1} \iff \Phi = \frac{1-\phi_p}{n\phi_p} S_i \ (i = w, oil) \tag{5}$$

where n is given by Eq. (2).

In our previous study [27], Eq. (3) and the developed theoretical model of yield stress was verified against data for *water*-continuous suspensions and very good agreement was obtained. Here, our goal is to extend this study to *oil*-continuous suspensions. First of all, experimental data for the yield stress, Y, vs. the relative fraction of inner (water) phase, S_w, are obtained for two oil phases of different interfacial tensions and viscosities (hexadecane and soybean oil). Comparison of results for Y, first, for the two different oil phases; second, for the two mirror systems (see Fig. 1) and, third, between the theoretical predictions and experimental data is carried out. The results indicate that in oil-continuous dispersions the attractive capillary-bridge force between the particles is partially counterbalanced by electrostatic repulsion across the oil phase, where there is no Debye screening of the electric field. The theory is generalized with the addition of electrostatic contribution to the interparticle force and the obtained model is verified against experimental data.

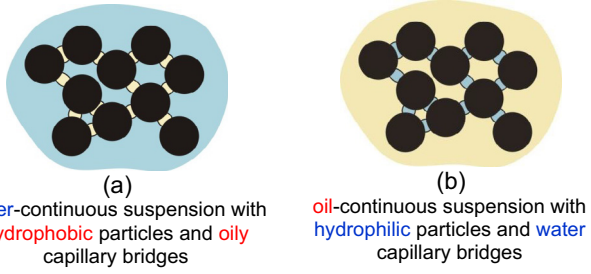

Fig. 1. Sketch of three-phase suspensions with capillary bridges: (a) water-continuous and (b) oil-continuous dispersion.

2. Materials and methods

2.1. Materials and procedures

All experiments were carried out at a room temperature of 25 ± 1 °C. Soybean oil (SBO) and hexadecane (C16) were used as oily phases. The soybean oil (SBO) from a local producer was purified by passing through a column filled with Silica gel (Merck, Germany) and activated magnesium silicate (Florisil, Sigma-Aldrich, Germany). The measured value of the SBO/water interfacial tension was $\sigma = 30$ mN/m and it did not decrease by more than 0.2 mN/m within 60 min. The measured viscosity of the purified SBO was 50 mPa s.

The hexadecane (Merck) has a density of 773 g/L and viscosity 3.0 mPa s. Before the experiments, the hexadecane was purified by passing it three times through a glass column filled with Silica gel and Florisil adsorbent. The measured interfacial tension of the purified C16 was $\sigma = 52$ mN/m. According to literature data [29], the relative dielectric constants of the two oils are $\varepsilon_{oil} = 2.05$ and 2.8 for the C16 and SBO, respectively.

The aqueous phase was deionized water (Elix purification system, Millipore) with dissolved 0.5 M NaCl (Merck), which was added to suppress the electrostatic interparticle repulsion across the water. No surfactants have been used in the aqueous phase.

In our experiments, we used hydrophilic silica particles Excelica UF320 produced by Tokuyama Corp., Japan, by melting of synthetic SiO_2 (density 2.2 g/cm^3). The particles were spherical, polydisperse, with low surface roughness and average particle diameter 3.8 μm; see Refs. [30–32]. To ensure high surface *hydrophilicity*, the following procedure for particle cleaning and activation was applied. First, the particles were stirred for 30 min, in aqueous solution of 1 wt% sodium hydroxide (NaOH). Then they were rinsed at least six times with deionized water to remove the NaOH. For this goal, laboratory centrifuge Sigma 3-16PK (for 4 min at 4000*g*) was used with removal of the supernatant. After that, the particles were spread as a thin layer in a Petri dish and dried at 120 °C for two hours. The dried particles were kept in a closed vessel to avoid condensation of water on their surfaces from the atmospheric air. To check the hydrophilicity of the particles thus prepared, a portion of them was sprinkled on the surface of the liquid in a cuvette containing an upper layer of oil (SBO or C16) and a lower layer of water. Under the action of their weight, the particles crossed the oil phase and the oil/water interface, and sank in the aqueous phase. This behavior indicates that the particle contact angle is $\alpha = 0°$. (In the case of finite contact angle, the particles would attach to the oil/water interface.) As already mentioned, such hydrophilic particles were used in *oil*-continuous suspensions with *water* capillary bridges.

In comparative experiments [27], we prepared *water*-continuous suspensions with *hydrophobic* particles and *oily* capillary bridges. For this goal, silica particles of the same kind were hydrophobized with hexamethyldisilazane (HMDS, 99%, Sigma Aldrich). First, the particles were heated to 800 °C for 30 min. After annealing in a desiccator with reduced humidity, the particles were brought into contact with vapors of HMDS under permanent stirring for 16 h. As a result of this pre-treatment, the silica particles become so hydrophobic that they do not enter the aqueous phase when placed on the air/water interface and subjected to agitation. If the particles and oil are simultaneously placed on the air/water interface, then it is possible to bring them into the aqueous phase by agitation. The contact angles of the hydrophobized particles were 168° and 110° across the water, respectively, in the cases of SBO and C16.

2.2. Experimental methods

The oil/water interfacial tensions were measured by using a pendant-drop tensiometer (instrument DSA30, Krüss GmbH, Germany). The three-phase contact angles of the hydrophobized particles were measured with bigger glass particles of radius 200–300 μm, hydrophobized in the same manner. The particles were floating on the oil/water interface and the contact angle was determined goniometrically, by side-view observations [33,34]. The suspensions were homogenized by using a propeller stirrer (Proxxon FBS 12/EF) with blending element from frappé mixer. The homogenization was performed at a rotation speed of 5000 rpm for 5 min. The rotation speed of such homogenizer does not depend on the hardness of the investigated capillary suspensions.

The rheological measurements were carried out using a rotational rheometer Bohlin Gemini, Malvern, UK, with geometry of two parallel disks. The upper disk is rotating, whereas the lower disk is immobile. Sheets of sandpaper of average particle diameter ≈12.6 μm were glued to both disks to prevent the appearance of wall slip. In the case of oil-continuous (water-continuous) suspension, the sandpaper was hydrophobized (hydrophilic). The disk radius was $R = 20$ mm. The investigated suspension was sandwiched between the two disks at a gap distance of 2 mm. The rotational rheometer measures the moment of force (torque) M acting on the rotating disk. Next, the average shear stress (force per unit area) acting on the rotating disk is calculated from the equation $\tau = 3M/(2\pi R^3)$; see Ref. [27] for more details.

3. Experimental results

3.1. Results for oil-continuous capillary suspensions

The rheological behavior of the capillary suspensions was studied using the *stress-control regime* of the rotational rheometer. In this regime, for each fixed value of the applied shear stress, τ, the strain characterized by the rotation angle, ψ, was measured; see Fig. 2. As seen in Fig. 2a, at the lower τ values the rotation angle ψ gradually increases. In double-logarithmic scale this dependence is linear, which implies that τ is a power function of ψ, viz. $\tau \propto \psi^{\nu}$. The average power for the four experiments shown in Fig. 2a is $\nu = 0.824 \pm 0.022$. Because $\nu \neq 1$, in Ref. [27] this regime was called *quasi-elastic* and was explained with the extension of capillary bridges upon shearing deformation.

At a certain value of τ, the angle ψ abruptly increases because the elastic limit has been reached. This value, $\tau = Y$, is identified with the *yield stress*. The respective value of the rotation angle, ψ_Y, represents the *yield strain*. In our experiments, Y was measured as a function of the relative volume fraction of the inner liquid (in this case – water), S_w, at different particle volume fractions, ϕ_p. The yield stress Y can be determined more accurately if the data are plotted in linear scale; see Fig. 2b.

Fig. 3 shows our data for Y vs. S_w for continuous phase of soybean oil (SBO) at $\phi_p = 35\%$, 40% and 45%. (At $\phi_p = 50\%$, the dispersion was too hard and inappropriate for investigation with the used rheometer.) Each point is average from at least three measurements, which have been carried out with separately prepared suspension samples of the same S_w and ϕ_p. The data indicate that the yield stress, Y, increases with the rise of both S_w and ϕ_p. For example, at $S_w = 3\%$ we have $Y = 1295$, 2460 and 4398 Pa for $\phi_p = 35\%$, 40% and 45%, respectively. Such increase of Y with ϕ_p is typical for jammed suspensions [35]. The error bars in Fig. 3 illustrate the reproducibility of these experiments, which is in the range from 5% to 10%.

In Fig. 3, at the greatest experimental values of S_w, the dependence of Y on S_w becomes irregular, which can be interpreted as a transition from the pendular to the funicular state due to overlap of neighboring capillary bridges [2,4,27]. At $S_w \geq 20\%$, phase separation is observed: the dispersion is decomposed to aqueous and

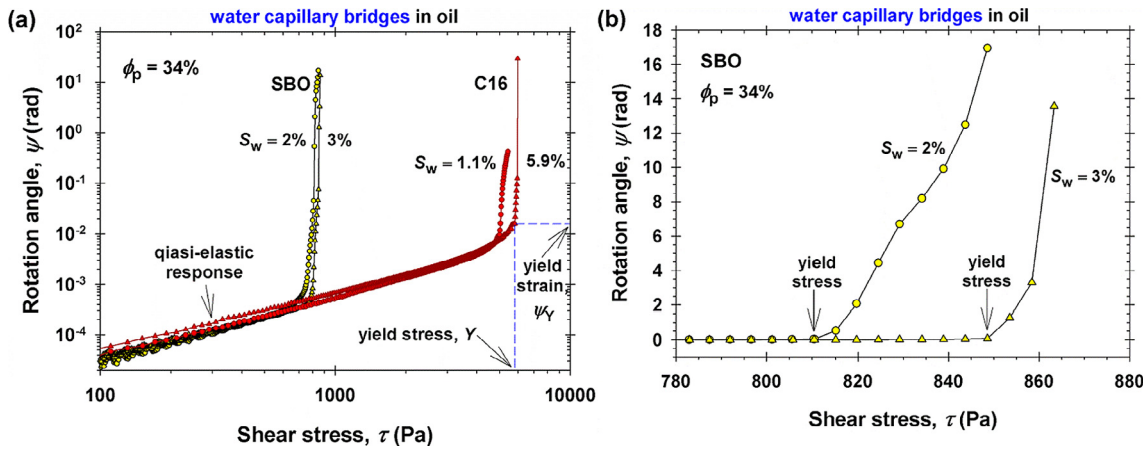

Fig. 2. Experimental data for the displacement angle, ψ, vs. the applied stress, τ, for four different values of S_w. (a) In double-logarithmic scale, one sees the power-law dependence between ψ and τ in the quasi-elastic regime. (b) In linear scale, the yield stress, Y, can be more accurately determined from the onset of steep rise of the experimental curve.

oil phases; the hydrophilic particles are located in the aqueous phase. At that, the system becomes fluid and $Y = 0$. Analogous behavior, with transition to funicular state and phase separation has been observed in the inverse system (water-continuous suspensions with hydrophobic particles and oily capillary bridges), with the only difference that after the phase separation the hydrophobic particles remain in the oily phase [27].

Fig. 4 shows analogous data, but for a continuous phase of C16 (instead of SBO). The data for C16 and SBO are compared in the same graph. Because the experiments are much time and labor consuming, in the case of C16 we carried out only one experiment for each S_w and ϕ_p. (The reproducibility of this type of experiments has been already estimated in Fig. 3.) The experiment shows that the yield stress Y is considerably greater for C16 as compared to SBO. Because for both systems the contact angle is the same, $\alpha = 0°$, this difference is mostly due to the different interfacial tensions of the two oils against water: 52 mN/m for C16 versus 30 mN/m for SBO. (More detailed discussion can be found in Section 5.2 in relation to the different values of the geometrical coefficient c_g for C16 and SBO.)

3.2. Comparison of results for oil- and water-continuous suspensions

In Fig. 5 we compare data for Y vs. S_i for *water* capillary bridges in oil from the present study with analogous data for *oily* capillary bridges in water from our previous paper [27]. One could expect that the values of Y for these two "mirror" system should coincide insofar as the interfacial tension σ is the same irrespective of whether the water or oil phase is inside or outside the capillary bridge. However, the data in Fig. 5 indicate significant differences. For example, for the suspensions with C16, the yield stress Y is greater for the *water* capillary bridges (Fig. 5a, b), whereas for the suspensions with SBO, Y is greater for the *oily* capillary bridges (Fig. 5c, d).

The interpretation of these (at a first glance, contradictory) results demands analysis based on a quantitative theory, which is developed in the next section. Here, we give only a preliminary discussion and qualitative interpretation, whereas the quantitative explanation will be given in Section 5.

The computer calculations [27], show that the maximal projection of the capillary-bridge force on the shear plane, $f_{cap,max}(\Phi,\alpha)$, which determines the yields stress Y, see Eq. (3), essentially decreases with the rise of contact angle, α, measured across the liquid in the bridge. The decrease of $f_{cap,max}$ is small for $0 < \alpha < 20°$, but $f_{cap,max}$ fast decreases for $\alpha > 20°$; see Eq. (4) and Fig. S2a in Appendix B. Hence, the differences between the experimental curves in Fig. 5a, b can be due mostly to the differences between the contact angles: $\alpha = 0°$ for water capillary bridges between hydrophilic particles in C16 vs. $\alpha = 70°$ for capillary bridges of C16 between hydrophobic particles in water.

However, the effect of α on $f_{cap,max}$ could not explain the data in Fig. 5c, d, because for the hydrophilic particles on the SBO/water interface the contact angle is $\alpha = 0°$ across the water, whereas for the hydrophobic particles on the SBO/water interface $\alpha = 12°$ across the oil was measured. In this range of relatively small α, the effect of *contact angle* on f_{max} is small (see Fig. S2a in Appendix B) and could not explain why the oil-continuous dispersions with water capillary bridges are softer (with smaller Y) than the water-continuous dispersions with oily capillary bridges. A possible source of this difference could be the *different viscosities* of the continuous and disperse (bridge) phases, viz. 50 mPa s for SBO vs. 0.89 mPa s for water. In general, the formation of a greater number of smaller droplets upon stirring should facilitate the formation of more capillary bridges, which would lead to greater yield stress Y. From the theory and experiment on emulsification in turbulent regime, it is known that the diameter of the formed drops decreases with the rise of viscosity of the continuous phase; see Fig. 10 in Ref. [36]. Hence, we could expect smaller droplets and greater Y in the case of water capillary bridges in SBO-continuous emulsions. However, the data for Y in Fig. 5c, d show exactly the opposite trend. Thus, we arrive at the hypothesis for *electrostatic interaction* across the oil phase as a possible explanation of the observed effect.

In previous measurements with hydrophobized SiO_2 particles, it was established that negative charges are present at the particle/oil interface [37–39], as well as at the particle/air interface [30–32]. In such a case, the lower values of the yield stress Y for the oil-continuous suspensions (Fig. 5c, d) could be explained with electrostatic repulsion between the neighboring particles across the oil phase, in which the electrostatic interactions are not screened because of the absence of electrolyte in the oil. (We recall that in our experiments the aqueous phase contains 0.5 M NaCl, so that electrostatic interactions across the water are not expected.) The electrostatic repulsion opposes the attractive capillary-bridge force between the particles. Thus, the magnitude of the net attractive force (capillary attraction minus electrostatic repulsion) is smaller, which leads to lowering of the yield stress Y. In Section 4.3, the theoretical model is upgraded by taking into account the effect of electrostatic repulsion between the particles.

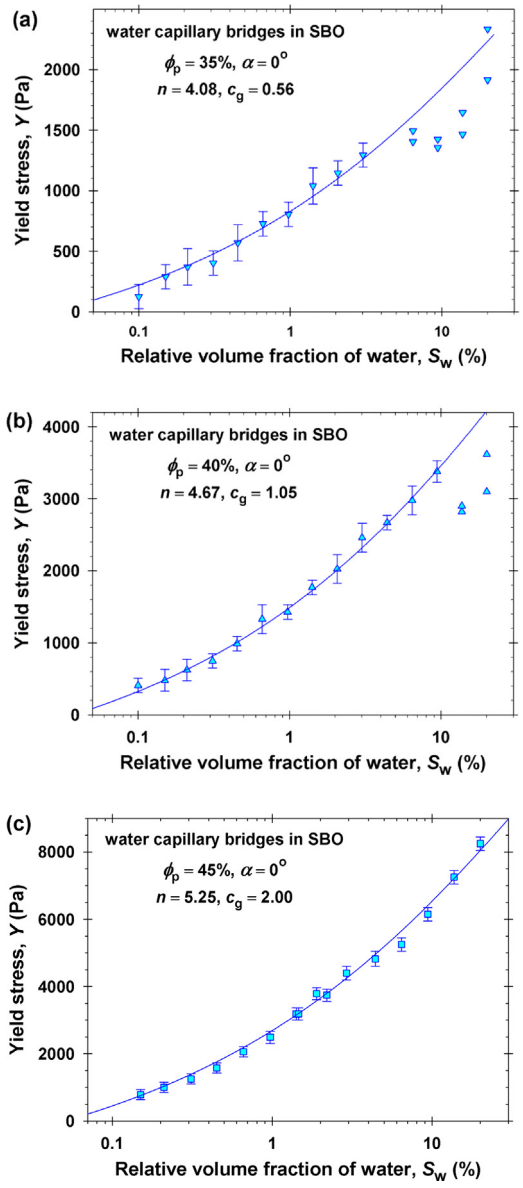

Fig. 3. Suspension with water capillary bridges in soybean oil (SBO): Plot of the measured yield stress, Y, vs. the relative volume fraction of water, S_w, for hydrophilic silica particles of volume fraction (a) ϕ_p = 35%; (b) ϕ_p = 40%, and (c) ϕ_p = 45%. The average number of capillary bridges per particle, n, is estimated from Eq. (2). The solid lines are fits by means of the theoretical model. The geometrical coefficient, c_g, is determined from the fit (details in the text).

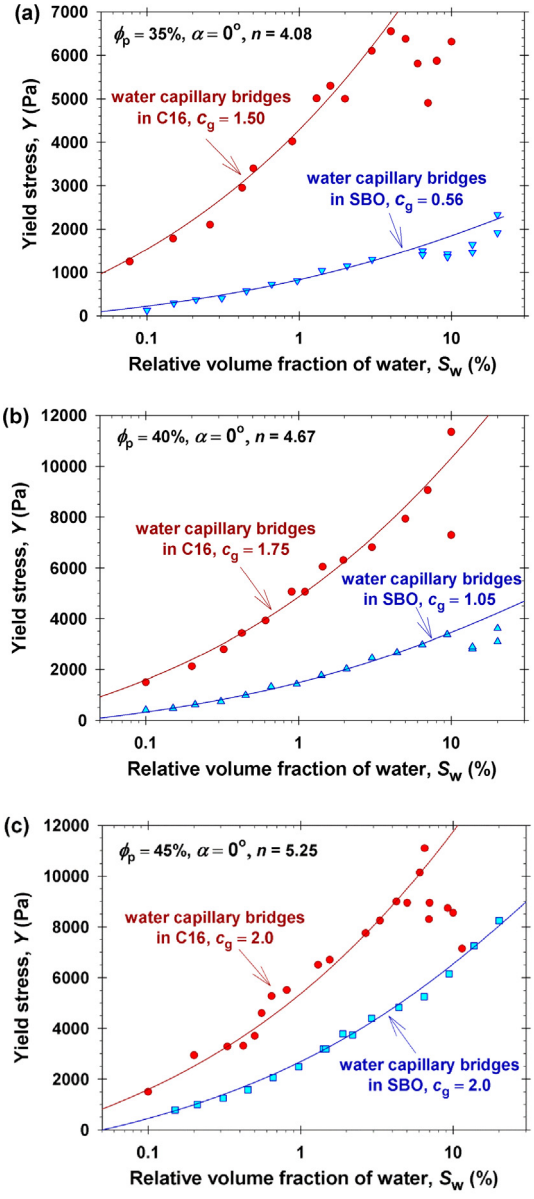

Fig. 4. Comparison of data for suspension with water capillary bridges in hexadecane (C16) and soybean oil (SBO): Plot of the measured yield stress, Y, vs. the relative volume fraction of water, S_w, for hydrophilic silica particles of volume fraction (a) ϕ_p = 35%; (b) ϕ_p = 40%, and (c) ϕ_p = 45%. The average number of capillary bridges per particle, n, is estimated from Eq. (2). The solid lines are fits by means of the theoretical model. The geometrical coefficient, c_g, is determined from the fit (details in the text).

4. Theoretical model

4.1. Capillary bridges and capillary force between particles

To calculate the shape of the capillary bridge and the capillary-bridge force between two equally-sized spherical particles, we used the same equations and computational procedures as in our previous paper [27]. For reader's convenience, the equations and procedures are described in Appendix A.

Fig. 6a shows a spherical particle and the half of the capillary bridge that connects it with another particle of the same size; a and V_p are the particle radius and volume; r and z are cylindrical coordinates; r_c and z_c are the coordinate of the three-phase contact line on the particle surface; φ_c is the respective central angle ($\sin\varphi_c = r_c/a$); as before, α is the contact angle measured across the *bridge* phase; $\theta_c = \varphi_c + \alpha$ is the meniscus slope angle at the contact line; r_0 is the radius of the "neck" of the bridge; h is the surface-to-surface distance between the two particles. The dimensionless bridge volume (defined as the bridge volume scaled with the volume of the two adjacent particles) is:

$$\Phi = \frac{V_{bridge}}{2V_p} = \frac{V_i}{V_p} \tag{6}$$

where $V_i = V_{bridge}/2$ is the volume of the "inner liquid" in the half-bridge (Fig. 6a). Φ is related to the experimental relative volume fraction of the inner phase, S_i, by Eq. (5).

The computational procedure based on the exact theory of capillary bridges (Appendix A) allows one to calculate the meniscus profile $z(r)$ at given values of three parameters, which can be (i) r_c, h, and α, or (ii) h, Φ and α. Illustrative meniscus profiles $z(r)$ at

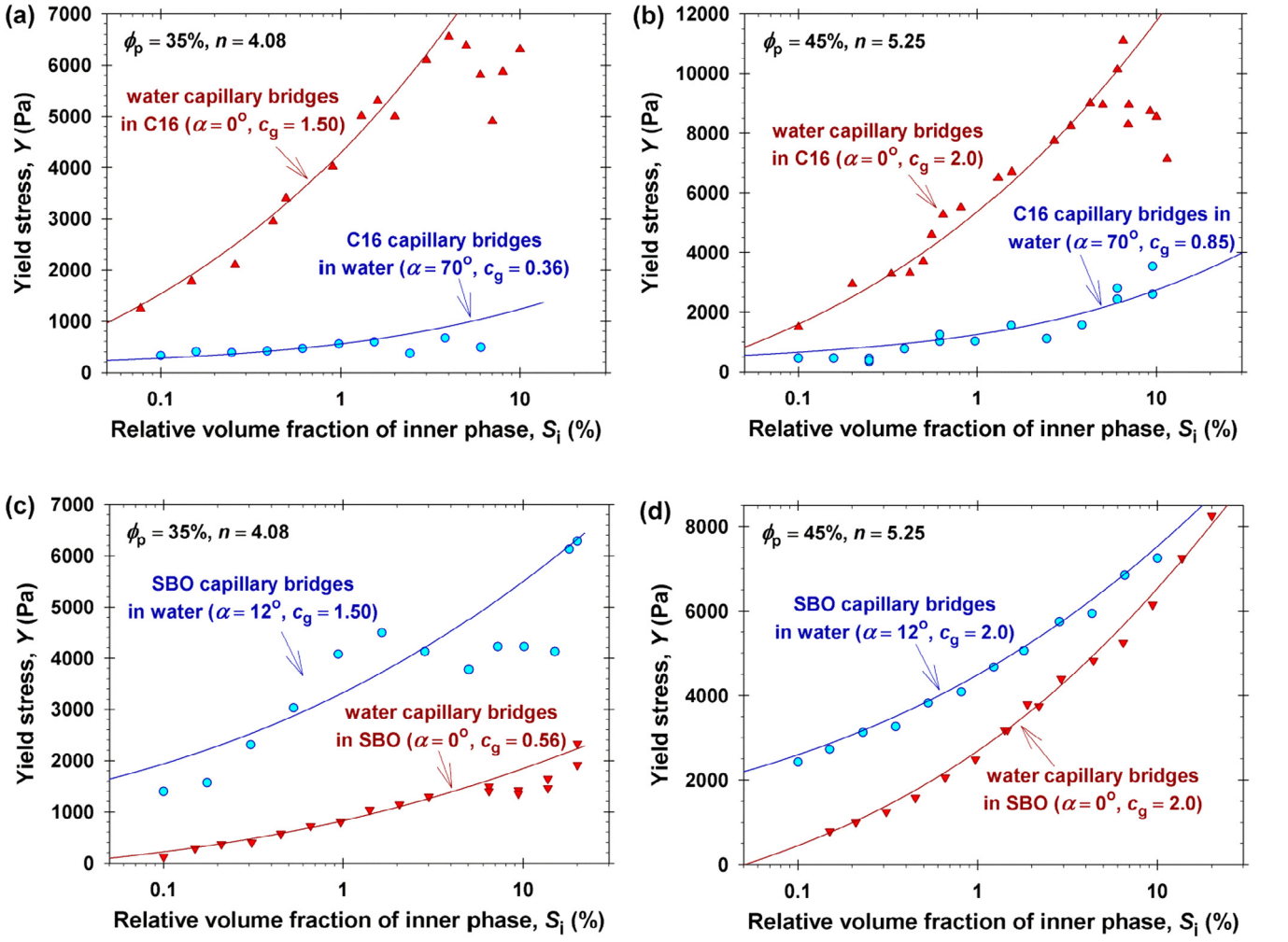

Fig. 5. Comparison of experimental data for the two inverse capillary suspensions with aqueous and oily capillary bridges at the same particle volume fraction ϕ_p: dependences of the yield stress, Y, on the relative volume fraction of the inner (bridge) phase, S_i, for: (a) ϕ_p = 35% and continuous phase of C16; (b) ϕ_p = 45% and continuous phase of C16; (c) ϕ_p = 35% and continuous phase of SBO, and (d) ϕ_p = 45% and continuous phase of SBO. The solid lines are fits by means of the theoretical model (details in the text).

various r_c values and fixed $\alpha = 0°$ and $h = 0$ (pendular rings) are shown in Fig. S1 in Appendix B. Meniscus profiles $z(r)$ at various h values and fixed $\Phi = 0.25$ and $\alpha = 0°$, are shown in Fig. 6b. We recall that $\alpha = 0°$ is the contact angle of our hydrophilized silica particles at the SBO/water and C16/water interfaces; see Section 3. Fig. 6b illustrates the variation of the meniscus profile upon extension of the capillary bridge (characterized by h) at fixed bridge volume (fixed Φ). In the initial state ($h = 0$, pendular ring between two particles in contact), the meniscus shape is cylindrical. Upon the increase of h (bridge extension), the bridge profile becomes more concave (the "neck" radius r_0 decreases) and the position of the contact line, (r_c,z_c), moves along the particle surface. For surface-to-surface distances that are greater than the "critical" value $h/(2a) = 0.7546$, the system of equations (Appendix A) has no solution for the given $\Phi = 0.25$. In other words, for greater values of $h/(2a)$ no equilibrium profile of the capillary bridge exists for the given volume.

Fig. 6c shows plots of the dimensionless capillary force, f_{cap}, vs. the dimensionless surface-to-surface distance, $\tilde{h}$, between two equal-sized particles; f_{cap} and $\tilde{h}$ are defined as follows:

$$f_{cap} = \frac{F_{cap}}{2\pi a\sigma}, \quad \tilde{h} = \frac{h}{2a} \tag{7}$$

where as usual, σ is the interfacial tension of the oil/water interface. The dimensionless capillary-bridge force, is an universal function, which depends on three parameters: $f_{cap} = f_{cap}(\tilde{h},\Phi,\alpha)$. In Fig. 6c, the contact angle is fixed, $\alpha = 0°$, whereas the dimensionless bridge volume, Φ, takes different fixed values for the different curves. It is interesting to note that at small values of $\tilde{h}$ the capillary force f_{cap} decreases with the rise of Φ, whereas at larger $\tilde{h}$ values the tendency is exactly the opposite. In Fig. 6c, each curve ends in a critical point; for greater values of $\tilde{h}$, the system of equations (Appendix A) has no solution and equilibrium capillary bridge does not exist for the given Φ.

4.2. Theoretical modeling of the yield stress

In Ref. [27], a general approach to the theoretical description of the yield stress was proposed and applied to capillary-bridge forces between the particles in a capillary suspension. Here, we briefly outline this approach and specify it for the case of counteracting capillary-bridge and electrostatic forces.

Let us consider two neighboring particles, A and B, in the suspension that interact via central force, F, which could be electrostatic, van-der-Waals and/or capillary-bridge force (Fig. 7a). A

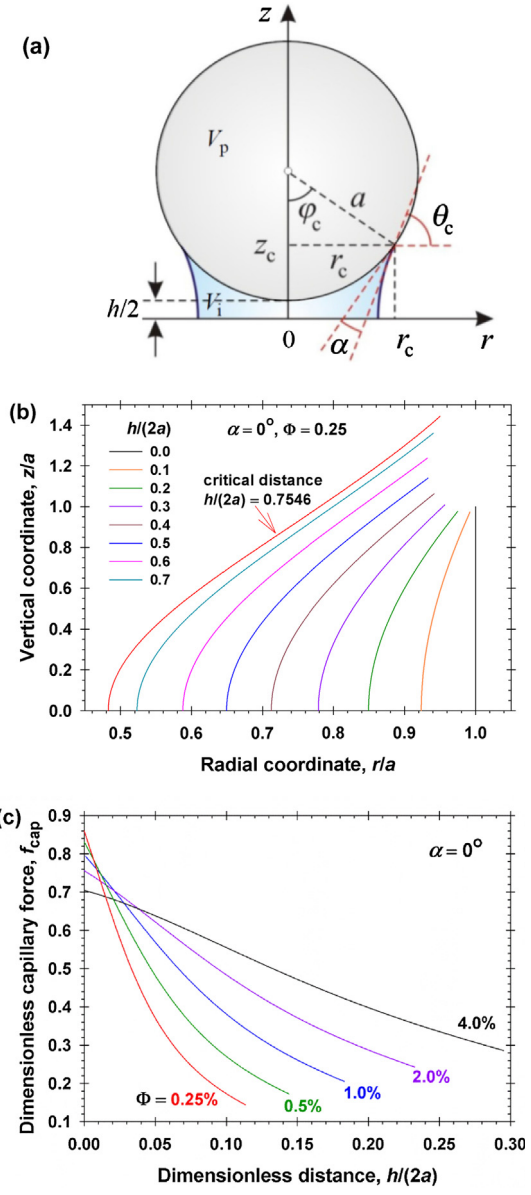

Fig. 6. (a) Capillary bridge between two equal-sized particles; half of the bridge is shown; h is the closest particle surface-to-surface distance; α is the three-phase contact angle measured across the bridge phase; r_c and z_c are the coordinates of the three-phase contact line; φ_c is the respective central angle; $\theta_c = \alpha + \varphi_c$ is the meniscus slope at the contact line; V_p is the particle volume; V_i is the volume of the "inner liquid" in the half-bridge; $\Phi = V_i/V_p$ is the dimensionless bridge volume. (b) Calculated profiles of a capillary bridge of fixed volume ($\Phi = 0.25$) at different degrees of extension (at different h) for $\alpha = 0°$. (c) Calculated dependences of the dimensionless capillary force, $f_{cap} = F_{cap}/(2\pi a\sigma)$, on the dimensionless surface-to-surface distance between the particles, $\bar{h} = h/(2a)$, at $\alpha = 0°$ and different Φ values.

small shear deformation of the suspension along the y-axis results in a displacement Δy of the particle B (Fig. 7b). The displacement leads to increase of the surface-to-surface distance between the particles A and B from h_0 to h. After the displacement, the central force F has non-zero projection on the shear plane:

$$F_{sh} \equiv F(h)\sin\gamma = F(h)\frac{\varepsilon}{(1+\varepsilon^2)^{1/2}} \tag{8}$$

where $\varepsilon = \Delta y/L = \tan\gamma$ (Fig. 7b). Using series expansions for small ε, we obtain:

$$h = [L^2 + (\Delta y)^2]^{1/2} - 2a = L(1+\varepsilon^2)^{1/2} - 2a$$
$$= h_0 + \frac{1}{2}L\varepsilon^2 + O(\varepsilon^4) \tag{9}$$

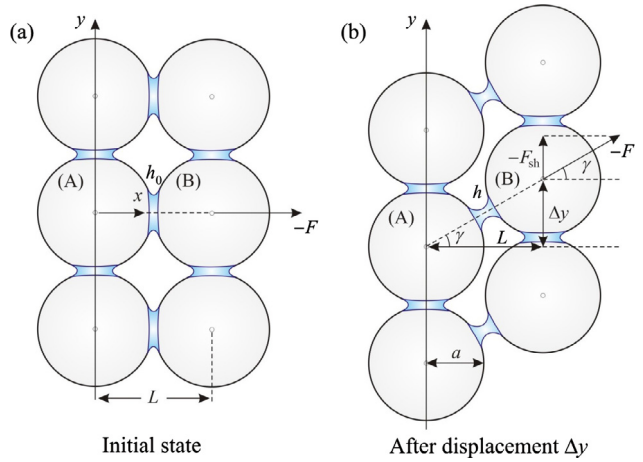

Fig. 7. Sketch of suspension from spherical particles of radius a connected by capillary bridges; (a) the initial state; (b) after a shear deformation at displacement Δy along the y-axis; L is the distance between two layers of particles; γ is the shearing angle; h_0 and h are the lengths of the capillary bridge before and after the shearing; F is the force of interaction between the particles A and B; $F_{sh} = F\sin\gamma$ is the projection of F on the shear plane.

$$F(h) = F(h_0) - \frac{1}{2}|F_h'|L\varepsilon^2 + O(\varepsilon^4),\ F_h' = \left.\frac{dF}{dh}\right|_{h=h_0} \tag{10}$$

where it has been assumed that the derivative F_h' is negative (i.e. that the magnitude of the net attractive force decrease with the distance h). In view of Eqs. (9) and (10), for small ε Eq. (8) acquires the form:

$$F_{sh}(\varepsilon) \approx F(h_0)\varepsilon - \frac{1}{2}[F(h_0) + |F_h'|L]\varepsilon^3 \tag{11}$$

The function $F_{sh}(\varepsilon)$ has a maximum at $\varepsilon = \varepsilon_m$, which is determined from the relation [27]:

$$\varepsilon_m = \frac{(2/3)^{1/2}}{[1 + |F_h'|L/F(h_0)]^{1/2}} \tag{12}$$

$$F_{sh,max} \approx \frac{2}{3}F(h_0)\varepsilon_m \tag{13}$$

For $F_{sh} < F_{sh,max}$, the system can counterbalance the applied external shear stress, i.e. we are dealing with quasi-elastic regime; see Fig. 2a. The value $F_{sh,max}$ corresponds to the *elastic limit* and is related to the *yield stress*. Note, that in the stress-control regime (used in our experiments), the yield stress is related to the maximum of $F_{sh}(\varepsilon)$, rather than to the stability limit of an extended capillary bridge. The yield stress Y can be expressed in the form [27]:

$$Y = c_g\phi_p^{2/3}\frac{F_{sh,max}}{\pi a^2} \tag{14}$$

where c_g is a geometrical coefficient, which accounts for the number of capillary bridges per particle and their orientation relative to the shear plane. In general, c_g could depend on ϕ_p. In capillary suspensions, c_g could depend on dynamic factors that influence the average number of capillary bridges per particle formed as a result of the stirring (homogenization) of the three-phase suspension [27].

For the investigated oil-continuous capillary suspensions, we assume that the force of interaction between two neighboring particles is a superposition of capillary-bridge attraction of magnitude F_{cap} and electrostatic repulsion of magnitude F_{el}. Then, in view of Eq. (8) we obtain:

$$F_{sh} = (F_{cap} - F_{el})\sin\gamma \tag{15}$$

where we have taken into account that the capillary and electrostatic forces are acting in the opposite directions.

The approximate expression for $F_{sh,max}$ in Eq. (13) is a result of series expansion, which is not always accurate. For this reason, in this article Y has been calculated from Eq. (14) along with Eq. (15), where F_{cap} has been computed using the exact theory of capillary bridges described in Appendix A. F_{el} has been calculated from an expression derived in Section 4.3. The maximum value $F_{sh,max}$ has been computed numerically.

4.3. Electrostatic repulsion across the oil phase

As already mentioned, the presence of 0.5 mM NaCl in the water suppresses the electrostatic interactions across the aqueous phase. In contrast, Debye screening is absent in the oil phase, so that the presence of electric charges (even at a low surface density) at the particle/oil interface gives rise to a strong electrostatic particle-particle repulsion across the oil phase. Such electrostatic repulsion across the nonpolar fluid (oil, air) leads to the formation of non-densely packed particle monolayers of hexagonal lattice on both oil/water and air/water interfaces [33,37–42]. It was established that the asymptotic electrostatic force, F_{el}, between two particles at the water/nonpolar fluid interface corresponds to repulsion between two *parallel* dipoles, for which $F_{el} \propto 1/L^4$ for $L \to \infty$, with L being the interparticle center-to-center distance [32,33,37,38,43]. The surface pressure of interfacial monolayers from charged particles has been also investigated and described theoretically [30–33,40].

In our experiments with oil-continuous suspensions and water capillary bridges, the volume fraction of water is between 0.1% and 10% relative to the total volume of the liquid phase (see S_w in Fig. 4), so that the volume fraction of oil is in the range between 90% and 99.9%. In such a case, electrostatic interparticle repulsion across the prevailing oil phase are very probable. As illustrated in Fig. 8a, this repulsion originates from electric charges located at the particle/oil interface; see e.g. Ref. [32]. Because the suspension is electroneutral and the charge density in the oil phase is practically zero, the counterions of the aforementioned surface charges have to be located in the water phase, i.e. at the surface of the capillary bridges where the force lines of electric field close. In first approximation, electric field of such geometry can be modelled as the field of two *antiparallel* dipoles interacting across the oil phase (Fig. 8). The force of repulsion between such two dipoles is:

$$F_{el} = \frac{3p_d^2}{2\pi\varepsilon_0\varepsilon_{oil}(b+h)^4} \tag{16}$$

where p_d is an effective dipole moment; ε_0 is the vacuum permittivity; ε_{oil} is the dielectric constant of the oil phase; $(b + h)$ is the distance between the two dipoles where $b/2$ is the distance between the effective dipole and particle surface, and (as before) h is the surface-to-surface distance between the two particles (Fig. 8b). Note that the repulsive force between two antiparallel dipoles is four times stronger that between two parallel dipoles separated at the same distance; see e.g. Eq. (4.5) in Ref. [44].

In our calculations, Eq. (16) has been used to estimate the electric force, F_{el}, in Eq. (15). It is convenient to introduce the following dimensionless variables:

$$f_{sh} = \frac{F_{sh}}{2\pi a\sigma} = (f_{cap} - f_{el})\sin\gamma \tag{17}$$

where f_{cap} is defined by Eq. (7) and

$$f_{el} = \frac{F_{el}}{2\pi a\sigma} = \frac{3p_d^2}{4\pi^2\varepsilon_0\varepsilon_{oil}b^4 a\sigma}\left(1+\frac{h}{b}\right)^{-4} \tag{18}$$

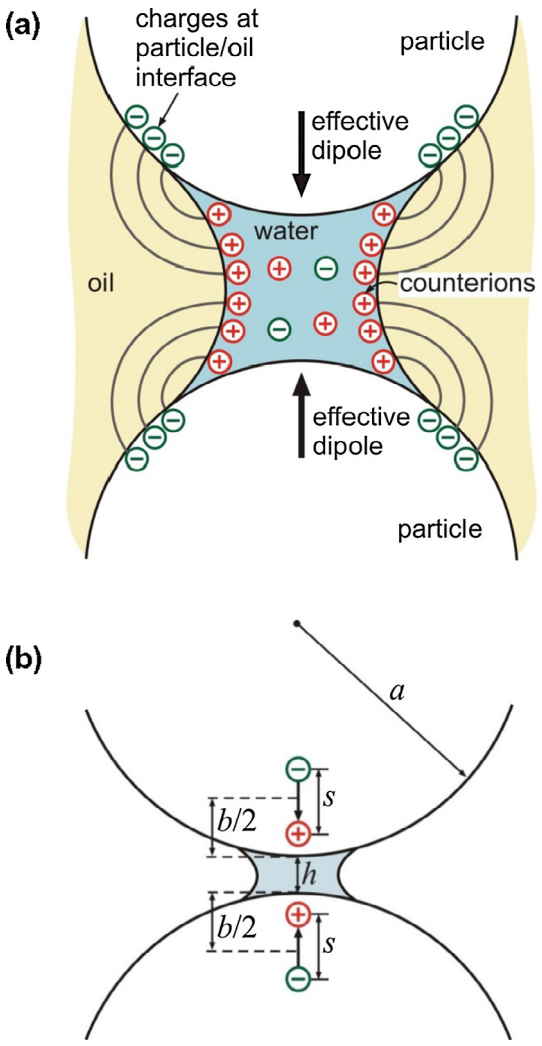

Fig. 8. (a) The surface charges at the particle/oil interface and their counterions in the water capillary bridge induce electric field, which is close to the field of two antiparallel effective dipoles (the size of the aqueous bridge is exaggerated). (b) In the proposed model, the effective dipoles are located at a distance $b/2$ from the particle surface and the characteristic dipole length is s.

The effective dipole moment p_d can be estimated as follows:

$$p_d = \frac{4\pi a^2\rho_{el}}{n}s \tag{19}$$

Here, ρ_{el} is the electric charge density at the particle/oil interface; the term $4\pi a^2\rho_{el}/n$ represents the particle surface charge per bridge, and s is a characteristic dipole length (Fig. 8b). To reduce the number of adjustable parameters, we will assume that b and s are inversely proportional to the mean number of capillary bridges per particle, n:

$$s = \frac{s_1}{n},\quad b = \frac{b_1}{n} \tag{20}$$

Substituting Eqs. (19) and (20) in Eq. (18), we obtain:

$$f_{el} = \frac{12a^3(\rho_{el}s_1)^2}{\varepsilon_0\varepsilon_{oil}b_1^4\sigma}\left(1+n\frac{h}{b_1}\right)^{-4} \tag{21}$$

In view of Eqs. (14) and (17), the yield stress is given by the expression:

$$Y = \frac{2\sigma}{a}c_g\phi_p^{2/3}f_{max} \tag{22}$$

The latter equation is analogous to Eq. (3), but in Eq. (22) f_{max} contains contributions from both capillary-bridge and electrostatic

forces; f_{max} is the maximal value of the shear response force f_{sh} defined by Eq. (17), where f_{cap} is to be calculated as explained in Appendix A and f_{el} is given by Eq. (21). In the latter equation, b_1 and $\rho_{el}s_1$ can be determined as adjustable parameters from the fit of experimental data. These two parameters do not depend on n and on the particle volume fraction ϕ_p. Hence, one could simultaneously fit all six experimental curves in Fig. 4 with the same values of b_1 and $\rho_{el}s_1$ (see below).

5. Numerical data and discussion

5.1. Comparison of theory and experiment

As illustrated in Fig. 7, the shear deformation leads to extension of capillary bridges, i.e. to increase of h. The relation between $\tilde{h} = h/(2a)$ and the shearing angle γ is [27]:

$$\tan\gamma = \left[(\tilde{h}+1)^2 - 1\right]^{1/2} \tag{23}$$

where it has been assumed that $h = 0$ at $\gamma = 0$ (i.e. $h_0 = 0$); see also Eq. (A.17) in Appendix A. The maximal shear-response force, f_{max}, has been determined numerically, as the maximum of the dependence of f_{sh} on γ at a given value of Φ; the latter is calculated from Eq. (5), along with Eq. (2), from the values of S_w and ϕ_p.

The theoretical curves in Figs. 3 and 4 have been drawn in the following way. For the curve for SBO-continuous suspension with water capillary bridges at $\phi_p = 45$ %, the value $c_g = 2.0$ is used, which is the same as for water-continuous dispersion with SBO bridges [27]. The following two parameters were determined from the fit:

$$\tilde{b}_1 \equiv \frac{b_1}{2a} = 2.52 \pm 0.01, \ \rho_{el}s_1 = 1.45 \times 10^{-8} \text{ C/m} \tag{24}$$

Furthermore, all other theoretical curves in Figs. 3 and 4 were drawn using the parameter values in Eq. (24), by variation of a single parameter, c_g. The values of c_g corresponding to the theoretical curves are compared in Table 1. In the same table, the values of n calculated from Eq. (2) and of $b/(2a)$ calculated from Eq. (20) with $b_1/(2a)$ from Eq. (24) are also shown.

The theoretical curves for the C16-continuous suspensions in Fig. 4 were drawn by using c_g values predicted by the empirical expression

$$c_g = 5\phi_p - 0.25 \tag{25}$$

which was obtained in Ref. [27]. In fact, good agreement between the experimental data and the theoretical curves for C16 was obtained without variation of any adjustable parameters.

In Table 1, the values of c_g are smaller for SBO in comparison with C16 (especially at $\phi_p = 0.35$ and 0.40). A possible explanation of this result could be that the viscosity of SBO is considerably higher than that of water (and of C16), which could have led to detachment of a part of the water capillary bridges from the particles during the stirring/preparation of the SBO-continuous dispersions.

The values of $b/(2a)$ in Table 1 indicate that the effective dipole is located near the middle of the distance between the particle center and surface (Fig. 8b), which is a physically reasonable result. With the increase of the number of bridges per particle, n, the dipole comes closer to the capillary bridge; $b/(2a)$ decreases, which reflects the fact that a smaller part of the particle surface (with its surface charges) contributes to the effective dipole moment.

Table 1
Comparison of parameter values corresponding to the theoretical curves in Figs. 3 and 4.

ϕ_p	n	$b/(2a)$	c_g	
			SBO	C16
0.35	4.08	0.618	0.56	1.50
0.40	4.67	0.540	1.05	1.75
0.45	5.25	0.480	2.00	2.00

To estimate the surface charge density at the particle/oil interface, ρ_{el}, we could assume that the dipole length is $s \approx b/2$; see Fig. 8b. In view of Eqs. (20) and (24), this means that $s_1 \approx b_1/2 = 4.84$ μm (in our experiments the mean particle radius is $a = 1.92$ μm). In view of Eq. (24), the obtained value of s_1 leads to $\rho_{el} = 0.30$ μC/cm^2. This value is close to the values obtained by Petkov et al. [30–32] for silica particles, and by Aveyard et al. [33] and Vermant et al. [40] for latex particles.

5.2. Theoretical predictions and discussion

Having determined the parameters of the system, we can estimate the interparticle forces, which determine the hardness of the capillary suspension and the yield stress, Y. First, let us consider the capillary component of the dimensionless shear-response force of the capillary suspension $f_{cap}\sin\gamma$. Fig. 9a shows plots of $f_{cap}\sin\gamma$ vs. the shearing angle (strain) γ. The different curves correspond to different fixed values of the dimensionless bridge volume, Φ, and the rise of γ induces extension of the capillary bridge. One sees that for each given Φ, the calculated curves have a maximum of height that increases with the rise of Φ. It should be noted that $f_{cap}(\gamma)$ is a monotonically decreasing curve (see Fig. 6c and Eq. (22)), so that the maxima in Fig. 9a are due to the second multiplier, $\sin\gamma$. As mentioned above, each theoretical curve has an end-point. At values of γ that are to the right of end-point, the system of equations in Appendix A has no physical solution for the given Φ. In such a case, equilibrium capillary bridge does not exist.

Fig. 9b illustrates the effect of the electrostatic repulsion on the f_{sh} vs. γ dependence; f_{el} is calculated from Eq. (21) with parameter values from Eq. (23) and $n = 5.25$. As seen in the figure, the electrostatic repulsion between the particles significantly decreases f_{max} and the related yield stress, Y; see Eq. (22). Moreover, Fig. S3 in Appendix B illustrates that with the increase of the bridge volume, Φ, the magnitude of the *capillary* component in f_{sh} increases, so that the relative contribution of the *electrostatic* interparticle repulsion to f_{max} and Y decreases.

Fig. 9c illustrates the dependence of the geometric coefficient c_g on the particle volume fraction, ϕ_p; see also Table 1. As already mentioned, the different $c_g(\phi_p)$ dependencies for SBO and C16 could be explained with dynamic effects related to the higher viscosity of SBO as compared to C16 (50 vs. 3 mPa s). The viscosity difference gives rise to two effects that are acting in opposite directions. First, if the outer liquid (e.g. SBO) has a higher viscosity than the inner liquid (e.g. water), then it is possible the friction forces during stirring to detach (to scrap away) capillary bridges from the particle surfaces, which would lead to decrease of c_g. Second, the higher viscosity of the outer liquid leads to splitting of the inner liquid to a greater number of smaller droplets [36]. This increases the probability for particle-droplet collision and capillary bridge formation, which tends to increase c_g. The first effect seems to prevail at lower ϕ_p, whereas the second – at higher ϕ_p. This could give an explanation of the stronger dependence of c_g on ϕ_p for SBO (Fig. 9c).

Finally, let us discuss the deviations of the experimental data from the theoretical curves at the higher S_w values; see Figs. 3 and 4. As mentioned above, these deviations could be explained with a transition from pendular to funicular state [2,27]. Physically, the onset of this transition is related to the overlap and merging of capillary bridges on the particle surface. In the case of simple cubic lattice with 6 bridges per particle (Fig. 7), two neighboring bridges do not overlap if the following relation is satisfied [27]:

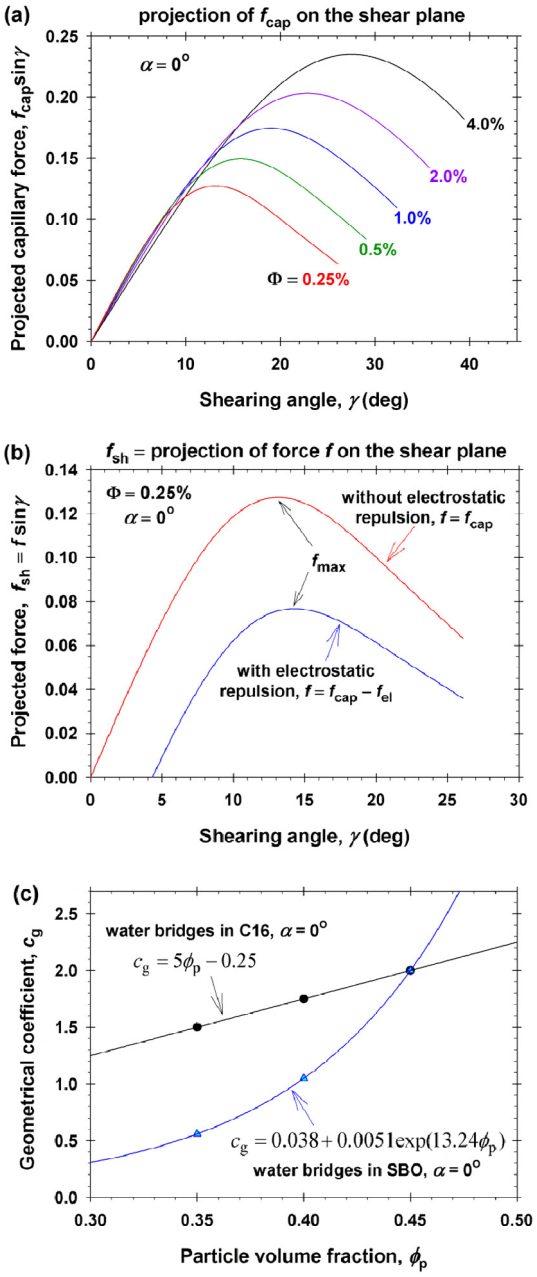

Fig. 9. (a) Calculated plots of the dimensionless capillary-bridge component of the shear response force, $f_{cap}\sin\gamma$, vs. the shearing angle γ at contact angle $\alpha = 0°$ and various values of the dimensionless bridge volume, Φ. (b) Comparison of plots of the shear-response force, f_{sh}, vs. γ without and with electrostatic repulsion; the other parameter values (n, ε_{oil}, σ and a) correspond to Fig. 3c. (c) Comparison of plots of the geometrical coefficient, c_g, vs. the particle volume fraction, ϕ_p, for the theoretical curves in Fig. 4.

$$\gamma + \varphi_c(h) + \varphi_c(0) < \frac{\pi}{2} \tag{26}$$

See Fig. S4 in Appendix B for the derivation of Eq. (26). In Fig. S5 therein, it is demonstrated that at the maximum of the f_{sh}-vs.-γ curve Eq. (26) is satisfied for Φ = 0.25% and 1%, but Eq. (26) is violated for Φ = 4%. In other words, for Φ = 4% the suspension is expected to be in the funicular state. To compare this theoretical prediction with the experimental results in Fig. 3, we calculated the values of S_w corresponding to Φ = 4%. For this goal, we used the equation

$$S_w = \frac{11.67\phi_p^2}{1-\phi_p}\Phi \tag{27}$$

which follows from Eqs. (2) and (5). From Eq. (27) with Φ = 4%, we estimate that deviations from the pendular state for ϕ_p = 0.35, 0.40 and 0.45 should appear, respectively, at S_w = 8.8%, 12.5% and 17.2%, which is in agreement with the data in Fig. 3.

The effect of *contact-angle hysteresis*, which is present for both rough and molecularly smooth solid surfaces [45–47], also deserves discussion. The magnitude of contact angle, α, affects (i) the value of yield stress, Y, and (ii) the overlap of capillary bridges on particle surface, which determines the transition from pendular to funicular state. Under the dynamic conditions of suspension preparation by stirring, capillary bridges are continuously formed, expanded and broken. During such a process, it is more likely that the contact angle (established after the end of stirring) is closer to the receding angle across the bridge phase. So, better agreement between theory and experiment is to be expected if the value of receding angle is substituted for α. For the considered hydrophilic particles in oil-continuous dispersions, we have $\alpha = 0$ across water. As seen in Fig. S2a in Appendix B, for small contact angles the calculated effect of α on f_{max} is very small. For this reason, we do not expect a considerable effect of contact angle variation (hysteresis) on the values of Y for the oil-continuous dispersions with water capillary bridges, investigated in the present article. In addition, for $\alpha \approx 0$ any hysteresis would lead to greater contact angles, weaker bridge overlap, and broader interval of S_w values for the pendular state.

Another effect that should be discussed is the influence of *electrolyte concentration* in the aqueous phase on the hardness of capillary suspensions. In the case of *water*-continuous suspensions investigated in Ref. [27], the absence of electrolyte in the aqueous phase led to softer suspensions and to less reproducible data for Y, as compared to the case with 0.5 M NaCl in the water. For this reason, in our systematic experiments we worked with aqueous phase that contains 0.5 M NaCl. The effect of NaCl in the case of water-continuous suspensions could be attributed to the suppression of electrostatic barriers that hinder the contact of particles and oil droplets and the formation of capillary bridges. In the case of *oil*-continuous dispersions, we have worked only with aqueous phase that contains 0.5 M NaCl. The study of the effect of electrolyte concentration on the hardness of oil-continuous capillary suspensions (if such effect exists) could be a subject of a separate study.

The *dielectric constant* of the oil phase, ε_{oil}, could also influence the yield stress, Y, through the electrostatic force, F_{el}; see Eq. (16). Greater ε_{oil} would lead to smaller value of F_{el} and to harder suspensions. However, the data in Fig. 4 show exactly the opposite tendency – Y is greater for the suspensions with C16, despite the lower ε_{oil} of C16 (as compared to SBO). In this case, the effect of interfacial tension on the capillary-bridge force is predominant – the greater Y for the suspensions with C16 is due to the higher interfacial tension: σ = 52 mN/m for C16 vs. 30 mN/m for SBO. Quantitatively, the electrostatic contribution to Y is characterized by Eq. (18), where the product $\varepsilon_{oil}\sigma$ appears in the denominator.

6. Conclusions

The particle/oil/water three-phase capillary suspensions possess the remarkable property to solidify upon the addition of minimal amount of the inner (dispersed) liquid. Most of the previous works on such suspensions investigate the 10–30 vol% range of particle concentrations, where particles and capillary menisci form networks with large voids that are free of particles [4,6]. In a recent study [27], we investigated uniform capillary suspensions (without voids) in the relatively weakly studied concentration range of 30–55 vol% particles. The hardening of these suspensions was due to the formation of capillary bridges (pendular rings), which connect the particles. Theoretical model of the yield stress was developed,

which is in good agreement with experimental data for *water*-continuous dispersions with hydrophobic particles and oily capillary bridges (pendular state).

In the present article, the main novelties are (i) that the study from Ref. [27] is extended to the "mirror" system of *oil*-continuous suspension with hydrophilic particles and water capillary bridges, and (ii) that the effect of *electrostatic* particle-particle repulsion across the oily phase is described theoretically and taken into account for data interpretation. (The electrostatic repulsion across the aqueous phase is suppressed because of the presence of 0.5 M NaCl.) The mechanical strength of dispersions is characterized by the yield stress Y, which is measured as a function of the volume fraction of the aqueous phase at various particle volume fractions. Experiments with two different oils, mineral (hexadecane) and vegetable (soybean oil), have been carried out. It is established that the yield stress (and the suspension's hardness) increases with the rise of the volume fractions of capillary bridges, S_w, and particles, ϕ_p.

For the studied *oil-continuous* suspensions, it is established that the yield stress Y is higher for the suspensions with hexadecane in comparison with those with soybean oil, all other conditions being the same (Fig. 4). This can be explained with a predominant effect from the higher hexadecane/water interfacial tension.

For the capillary suspensions with *hexadecane*, the comparison of the "mirror" systems of water- and oil-continuous dispersions shows that Y is *higher* for the oil-continuous suspensions, which could be explained with a predominant effect from the contact-angle difference, 0° vs. 70° (Fig. 5a, b).

In contrast, for the capillary suspensions with *soybean oil*, the comparison of the "mirror" systems of water- and oil-continuous dispersions shows that Y is *lower* for the oil-continuous suspensions, which cannot be explained with contact-angle differences (Fig. 5c, d). A possible explanation of this result is the existence of interparticle electrostatic repulsion across the oil phase, where there is no Debye screening of the electric field. Such repulsion across the oil phase has been observed in monolayers of silica and latex particles spread on the oil-water interface [33–35,37–40].

To verify this hypothesis, we upgraded the theoretical model from Ref. [27] by taking into account the contribution from electrostatic repulsion, which partially counterbalances the capillary-bridge attraction and renders the capillary suspensions softer. The particle charge density determined from fits of experimental data for Y is close to the values obtained by other authors [30–33,40]. This fact supports the hypothesis for the essential effect of electrostatic interactions on the hardness of oil-continuous capillary suspensions. The results of the present study could contribute for a better understanding, quantitative prediction and control of the mechanical properties of solid/liquid/liquid three-phase suspensions.

Acknowledgements

The authors gratefully acknowledge the support from Unilever R&D and from the Horizon 2020 project ID: 692146-H2020-eu.4.b "Materials Networking".

Appendix A. Supplementary material

Appendix A "System of equations and computational procedure" and Appendix B "Additional experimental and computational results" are presented as Supplementary data associated with this article can be found, in the online version, at https://doi.org/10.1016/j.jcis.2017.11.057.

References

[1] H. Schubert, Capillary force-modeling and application in particulate technology, Powder Technol. 37 (1984) 105–116.
[2] N. Mitarai, F. Nori, Wet granular materials, Adv. Phys. 55 (2006) 1–45.
[3] E. Koos, N. Willenbacher, Capillary forces in suspension rheology, Science 331 (2011) 897–900.
[4] E. Koos, Capillary suspensions: particle networks formed through the capillary force, Curr. Opin. Colloid Interface Sci. 19 (2014) 575–584.
[5] T. Domenech, S.S. Velankar, On the rheology of pendular gels and morphological developments in paste-like ternary systems based on capillary attraction, Soft Matter 11 (2015) 1500–1516.
[6] F. Bossler, E. Koos, Structure of particle networks in capillary suspensions with wetting and nonwettining fluids, Langmuir 32 (2016) 1489–1501.
[7] F.M. Orr, L.E. Scriven, A.P. Rivas, Pendular rings between solids: meniscus properties and capillary force, J. Fluid Mech. 67 (1975) 723–742.
[8] P.A. Kralchevsky, K. Nagayama, Particles at Fluid Interfaces and Membranes, Elsevier, Amsterdam, Chapters 2 and 11, 2001.
[9] T.I. Vogel, Liquid bridges between contacting balls, J. Math. Fluid Mech. 16 (2014) 737–744.
[10] K. Stratford, R. Adhikari, I. Pagonabarraga, J.-C. Desplat, M.E. Cates, Colloidal jamming at interfaces: a route to fluid-bicontinuous gels, Science 309 (2005) 2198–2201.
[11] E.M. Herzig, K.A. White, A.B. Schofield, W.C.K. Poon, P.S. Clegg, Bicontinuous emulsions stabilized solely by colloidal particles, Nat. Mater. 6 (2007) 966–971.
[12] K.A. White, A.B. Schofield, B.P. Binks, P.S. Clegg, Influence of particle composition and thermal cycling on bijel formation, J. Phys. Condens. Matter 20 (2008) 494223.
[13] M.F. Haase, N. Sharifi-Mood, D. Lee, K.J. Stebe, In situ mechanical testing of nanostructured bijel fibers, ACS Nano 10 (2016) 6338–6344.
[14] S. Hoffmann, E. Koos, N. Willenbacher, Using capillary bridges to tune stability and flow behavior of food suspensions, Food Hydrocolloids 40 (2014) 44–52.
[15] S. Wollgarten, C. Yuce, E. Koos, N. Willenbacher, Tailoring flow behavior and texture of water based cocoa suspensions, Food Hydrocolloids 52 (2016) 167–174.
[16] B. Bitsch, J. Dittmann, M. Schmitt, P. Scharfer, W. Schabel, N. Willenbacher, A novel slurry concept for the fabrication of lithium-ion battery electrodes with beneficial properties, J. Power Sources 265 (2014) 81–90.
[17] M. Schneider, E. Koos, N. Willenbacher, Highly conductive, printable pastes from capillary suspensions, Sci. Rep. 6 (2016) 31367.
[18] B. Bitsch, T. Gallasch, M. Schroeder, M. Börner, M. Winter, N. Willenbacher, Capillary suspensions as beneficial formulation concept for high energy density Li-ion battery electrodes, J. Power Sources 328 (2016) 114–123.
[19] L. Jampolski, A. Sänger, T. Jakobs, G. Guthausen, T. Kolb, N. Willenbacher, Improving the process ability of coke water slurries for entrained flow gasification, Fuel 185 (2016) 102–111.
[20] W. Dapeng, X. Wang, Y. Yuan, W. Li, H. Tian, S. Zhao, Increasing the apparent shear viscosity of polymer composites by uptake of a small amount of water, RSC Adv. 4 (2014) 24686–24691.
[21] T. Domenech, S. Velankar, Capillary-driven percolating networks in ternary blends of immiscible polymers and silica particles, Rheol. Acta 53 (2014) 593–605.
[22] S. Heidlebaugh, T. Domenech, S. Iasella, S.S. Velankar, Aggregation and separation in ternary particle/oil/water systems with fully-wettable particles, Langmuir 30 (2014) 63–74.
[23] J. Dittmann, E. Koos, N. Willenbacher, Ceramic capillary suspensions: novel processing route for macroporous ceramic materials, J. Am. Ceram. Soc. 96 (2013) 391–397.
[24] J. Dittmann, N. Willenbacher, Micro structural investigations and mechanical properties of macro porous ceramic materials from capillary suspensions, J. Am. Ceram. Soc. 97 (2014) 3787–3792.
[25] J. Maurath, J. Dittmann, N. Schultz, N. Willenbacher, Fabrication of highly porous glass filters using capillary suspension processing, Sep. Purif. Technol. 149 (2015) 470–478.
[26] H. Sun, M.M.F. Yuen, Conductivity enhancement of thermal interface material via capillary attraction, in: IEEE 66th Electronic Components and Technology Conference (ECTC), 2016, pp. 1409–1414, doi: 10.1109/ECTC.2016.94.
[27] K.D. Danov, M.T. Georgiev, P.A. Kralchevsky, G.M. Radulova, T.G. Gurkov, S.D. Stoyanov, E.G. Pelan, Hardening of particle/oil/water suspensions die to capillary bridges: experimental yield stress and theoretical interpretation, Adv. Colloid Interface Sci. (2017), https://doi.org/10.1016/j.cis.2017.11.004.
[28] A. Goyal, C.K. Hall, O.D. Velev, Phase diagram for stimulus-responsive materials containing dipolar colloidal particles, Phys. Rev. E 77 (2008) 031401.
[29] P. Muley, D. Boldor, Investigation of microwave dielectric properties of biodiesel components, Bioresour. Technol. 127C (2012) 165–175.
[30] P.V. Petkov, K.D. Danov, P.A. Kralchevsky, Surface pressure isotherm for a monolayer of charged colloidal particles at a water/nonpolar-fluid interface: experiment and theoretical model, Langmuir 30 (2014) 2768–2778.
[31] P.V. Petkov, K.D. Danov, P.A. Kralchevsky, Monolayers from charged particles in a Langmuir trough: Could particle aggregation increase the surface pressure?, J Colloid Interface Sci. 462 (2016) 223–234.
[32] P.A. Kralchevsky, K.D. Danov, P.V. Petkov, Soft electrostatic repulsion in particle monolayers at liquid interfaces: surface pressure and effect of aggregation, Phil. Trans. R. Soc. A 374 (2016) 20150130.

[33] R. Aveyard, J.H. Clint, D. Nees, V.N. Paunov, Compression and structure of monolayers of charged latex particles at air/water and octane/water interfaces, Langmuir 16 (2000) 1969–1979.
[34] K.D. Danov, P.A. Kralchevsky, M.P. Boneva, Electrodipping force acting on solid particles at a fluid interface, Langmuir 20 (2004) 6139–6151.
[35] L. Botto, K. Preuss, L.X. Robertson, X.Y. Xu, Physical characterisation and yield stress of a concentrated *Miscanthus* suspension, Rheol. Acta 53 (2014) 805–815.
[36] N. Vankova, S. Tcholakova, N.D. Denkov, I.B. Ivanov, V.D. Vulchev, T. Danner, Emulsification in turbulent flow: 1. Mean and maximum drop diameters in inertial and viscous regimes, J. Colloid Interface Sci. 312 (2007) 363–380.
[37] T.S. Horozov, R. Aveyard, J.H. Clint, B.P. Binks, Order-disorder transition in monolayers of modified monodisperse silica particles at the octane-water interface, Langmuir 19 (2003) 2822–2829.
[38] T.S. Horozov, B.P. Binks, Particle behavior at horizontal and vertical fluid interfaces, Colloids Surf. A 267 (2005) 64–73.
[39] T.S. Horozov, R. Aveyard, B.P. Binks, J.H. Clint, Structure and stability of silica particle monolayers at horizontal and vertical octane–water interfaces, Langmuir 21 (2005) 7405–7412.
[40] S. Reynaert, P. Moldenaers, J. Vermant, Control over colloidal aggregation in monolayers of latex particles at the oil-water interface, Langmuir 22 (2006) 4936–4945.
[41] M.A. Ray, L. Jia, Micropatterning by non-densely packed interfacial colloidal crystals, Adv. Mater. 19 (2007) 2020–2022.
[42] B.J. Park, J.P. Pantina, E.M. Furst, M. Oettel, S. Reynaert, J. Vermant, Direct measurements of the effects of salt and surfactant on interaction forces between colloidal particles at water-oil interfaces, Langmuir 24 (2008) 1686–1694.
[43] K.D. Danov, P.A. Kralchevsky, Electric forces induced by a charged colloid particle attached to the water-nonpolar fluid interface, J. Colloid Interface Sci. 298 (2006) 213–231.
[44] T.D. Gurkov, P.A. Kralchevsky, K. Nagayama, Formation of dimers in lipid monolayers, Colloid Polym. Sci. 274 (1996) 227–238.
[45] V.M. Starov, Equilibrium and hysteresis contact angles, Adv. Colloid Interface Sci. 39 (1982) 147–173.
[46] A. Marmur, Thermodynamic aspects of contact angle hysteresis, Adv. Colloid Interface Sci. 50 (1994) 121–141.
[47] D. Brutin, V. Starov, Recent advances in droplet wetting and evaporation, Chem. Soc. Rev. (2018), https://doi.org/10.1039/C6CS00902F.

Supplementary material

for the article

Rheology of particle/water/oil three-phase dispersions: Electrostatic vs. capillary bridge forces

Mihail T. Georgiev [a], Krassimir D. Danov [a], Peter A. Kralchevsky [a,*], Theodor D. Gurkov [a], Denitsa P. Krusteva [a], Luben N. Arnaudov [b], Simeon D. Stoyanov [b,c,d], Eddie G. Pelan [b]

[a] *Department of Chemical & Pharmaceutical Engineering, Faculty of Chemistry and Pharmacy, Sofia University, Sofia 1164, Bulgaria*

[b] *Unilever Research & Development Vlaardingen, 3133AT Vlaardingen, The Netherlands*

[c] *Laboratory of Physical Chemistry and Colloid Science, Wageningen University, 6703 HB Wageningen, The Netherlands*

[d] *Department of Mechanical Engineering, University College London, WC1E 7JE, UK*

(The numbers of references are the same as in the main text of the article)

Appendix A. System of equations and computational procedure

1. Basic equations

The computational procedure used in this paper is a slightly modified and upgraded version of the procedure developed in Ref. [27]. For the computations, it is convenient to scale all quantities with dimension of length using the particle radius, a; the dimensionless quantities will be denoted by tilde:

$$\widetilde{r}=\frac{r}{a},\ \widetilde{z}=\frac{z}{a},\ \widetilde{r}_{\mathrm{c}}=\frac{r}{a},\ \widetilde{z}_{\mathrm{c}}=\frac{r}{a},\ \widetilde{r}_0=\frac{r_0}{a},\ \widetilde{h}=\frac{h}{2a},\ \widetilde{b}_{\mathrm{l}}\equiv\frac{b_{\mathrm{l}}}{2a} \tag{A.1}$$

For the meaning of the geometrical parameters, see Figs. 6a, 8b and Eq. (20) in the main text.

Here, our goals are to compute (i) the profile of the capillary bridges; (ii) the dimensionless capillary-bridge force, $f_{\mathrm{cap}} = f_{\mathrm{cap}}(\gamma,\Phi,\alpha)$; (iii) the dimensionless electrostatic force, $f_{\mathrm{el}} = f_{\mathrm{el}}(\gamma)$, the dimensionless shear-response force, $f_{\mathrm{sh}}(\gamma) = f_{\mathrm{cap}}(\gamma) - f_{\mathrm{el}}(\gamma)$, and the maximum value of f_{sh} with respect to γ, $f_{\max} = f_{\mathrm{sh,max}}$. As in the main text, h is the surface-to-surface distance between the two spherical particles connected by the capillary bridge; $\Phi = V_{\mathrm{i}}/V_{\mathrm{p}}$ is the dimensionless bridge volume, see Fig. 6a in the main text; α is the three-phase contact angle measured across the bridge phase, and γ is the shearing angle (Fig. 7b).

As demonstrated in Ref. [27], the dimensionless bridge profile $\widetilde{z}(x)$ can be calculated using the equations:

$$x = \left| \tilde{r} / \tilde{r}_0 - 1 \right|^{1/2} \tag{A.2}$$

$$\tilde{z}(x) = 2\tilde{r}_0 \int_0^x \frac{1 + p\xi^2(2+\xi^2)}{[(2+\xi^2)(1-2p-2p^2\xi^2-p^2\xi^4)]^{1/2}} \,\mathrm{d}\xi \quad (p < 0.5) \tag{A.3a}$$

$$\tilde{z}(x) = 2\tilde{r}_0 \int_0^x \frac{1 - p\xi^2(2-\xi^2)}{[(2-\xi^2)(2p-1-2p^2\xi^2+p^2\xi^4)]^{1/2}} \,\mathrm{d}\xi \quad (p > 0.5) \tag{A.3b}$$

The dimensionless bridge pressure, p, and capillary-bridge force, f_{cap}, are given by the expressions [27]:

$$p = \frac{\tilde{r}_0^2 - \tilde{r}_0 \tilde{r}_\mathrm{c} \sin\theta_\mathrm{c}}{\tilde{r}_0^2 - \tilde{r}_\mathrm{c}^2} \tag{A.4}$$

$$f_{\mathrm{cap}} = (1-p)\tilde{r}_0 \tag{A.5}$$

At the contact line on the particle surface, $(r, z) = (r_\mathrm{c}, z_\mathrm{c})$, Eqs. (A.2)–(A.3) acquire the form:

$$x_\mathrm{c} = \left| \tilde{r}_\mathrm{c} / \tilde{r}_0 - 1 \right|^{1/2} \tag{A.6}$$

$$\tilde{z}_\mathrm{c} = 2\tilde{r}_0 \int_0^{x_\mathrm{c}} \frac{1 + p\xi^2(2+\xi^2)}{[(2+\xi^2)(1-2p-2p^2\xi^2-p^2\xi^4)]^{1/2}} \,\mathrm{d}\xi \quad (p < 0.5) \tag{A.7a}$$

$$\tilde{z}_\mathrm{c} = 2\tilde{r}_0 \int_0^{x_\mathrm{c}} \frac{1 - p\xi^2(2-\xi^2)}{[(2-\xi^2)(2p-1-2p^2\xi^2+p^2\xi^4)]^{1/2}} \,\mathrm{d}\xi \quad (p > 0.5) \tag{A.7b}$$

The volume confined between the surface of the capillary bridge and the two horizontal planes $z = 0$ and $z = z_\mathrm{c}$ (see Fig. 6a), is:

$$V_\mathrm{c} = \pi \int_0^{z_\mathrm{c}} r^2 \,\mathrm{d}z = \pi \int_{r_0}^{r_\mathrm{c}} r^2 \frac{\mathrm{d}z}{\mathrm{d}r} \mathrm{d}r \tag{A.8}$$

Likewise, the area of the capillary meniscus of the bridge is:

$$A_\mathrm{c} = 2\pi \int_0^{z_\mathrm{c}} \frac{r}{\sin\theta} \,\mathrm{d}z = 2\pi \int_{r_0}^{r_\mathrm{c}} \frac{r}{\sin\theta} \frac{\mathrm{d}z}{\mathrm{d}r} \,\mathrm{d}r; \quad \sin\theta = p\frac{r}{r_0} + (1-p)\frac{r_0}{r} \tag{A.9}$$

Next, we introduce dimensionless variables in accordance with Eq. (A.1), express the derivative $\mathrm{d}\tilde{z} / \mathrm{d}x$ from Eq. (A.3). Thus, we obtain:

$$\tilde{V}_\mathrm{c} \equiv \frac{V_\mathrm{c}}{a^3} = 2\pi\tilde{r}_0^3 \int_0^{x_\mathrm{c}} \frac{[1 + px^2(2+x^2)](1+x^2)^2}{[(2+x^2)(1-2p-2p^2x^2-p^2x^4)]^{1/2}} \,\mathrm{d}x \quad (p < 0.5) \tag{A.10a}$$

$$\widetilde{V}_{\mathrm{c}} \equiv \frac{V_{\mathrm{c}}}{a^3} = 2\pi r_0^3 \int_0^{x_{\mathrm{c}}} \frac{[1 - px^2(2 - x^2)](1 - x^2)^2}{[(2 - x^2)(2p - 1 - 2p^2x^2 + p^2x^4)]^{1/2}} \mathrm{d}\, x \quad (p > 0.5) \tag{A.10b}$$

$$\widetilde{A}_{\mathrm{c}} = \frac{A_{\mathrm{c}}}{a^2} = 4\pi \widetilde{r}_0^2 \int_0^{x_{\mathrm{c}}} \frac{(1 + x^2)^2}{[(2 + x^2)(1 - 2p - 2p^2x^2 - p^2x^4)]^{1/2}} \mathrm{d}\, x \quad (p < 0.5) \tag{A.11a}$$

$$\widetilde{A}_{\mathrm{c}} = \frac{A_{\mathrm{c}}}{a^2} = 4\pi \widetilde{r}_0^2 \int_0^{x_{\mathrm{c}}} \frac{(1 - x^2)^2}{[(2 - x^2)(2p - 1 - 2p^2x^2 + p^2x^4)]^{1/2}} \mathrm{d}\, x \quad (p > 0.5) \tag{A.11b}$$

From Fig. 6a, we find the following relations between the geometrical parameters:

$$r_{\mathrm{c}} = a \sin\varphi_{\mathrm{c}}\,, \quad z_{\mathrm{c}} = \frac{h}{2} + a - a\cos\varphi_{\mathrm{c}}\,, \quad \theta_{\mathrm{c}} = \alpha + \varphi_{\mathrm{c}} \tag{A.12}$$

In view of Eq. (A.1), the dimensionless form of Eq. (A.12) is:

$$\widetilde{r}_{\mathrm{c}} = \sin\varphi_{\mathrm{c}}\,, \quad \widetilde{z}_{\mathrm{c}} = \widetilde{h} + 1 - \cos\varphi_{\mathrm{c}}\,, \quad \theta_{\mathrm{c}} = \alpha + \varphi_{\mathrm{c}} \tag{A.13}$$

The volume of the liquid in the upper part of the capillary bridge, V_{i}, is equal to the difference between V_{c} and the respective part of the particle volume (Fig. 6a):

$$V_{\mathrm{i}} = V_{\mathrm{c}} - \frac{\pi}{3}\left(z_{\mathrm{c}} - \frac{h}{2}\right)^2 \left(3a + \frac{h}{2} - z_{\mathrm{c}}\right) \tag{A.14}$$

Then, the dimensionless bridge volume, Φ, can be expressed in the form:

$$\Phi \equiv \frac{V_{\mathrm{i}}}{V_{\mathrm{p}}} = \frac{3V_{\mathrm{i}}}{4\pi a^3} = \frac{3\widetilde{V}_{\mathrm{c}}}{4\pi} - \frac{1}{4}(\widetilde{z}_{\mathrm{c}} - \widetilde{h})^2 (3 + \widetilde{h} - \widetilde{z}_{\mathrm{c}}) \tag{A.15}$$

What concerns the shear deformation we will assume that in the initial state the surfaces of the two particles touch each other (Fig. 7). Then, Eq. (9) in the main text with $L = 2a$ and $\varepsilon = \tan\gamma$ acquires the form:

$$h = 2a(1 + \tan^2\gamma)^{1/2} - 2a \tag{A.16}$$

From Eq. (A.16) we obtain an expression for determining γ:

$$\tan\gamma = [(\widetilde{h} + 1)^2 - 1]^{1/2} \tag{A.17}$$

which is Eq. (23) in the main text. In accordance with Eq. (17), (21) and (A.5), we have

$$f_{\mathrm{sh}} \equiv (f_{\mathrm{cap}} - f_{\mathrm{el}})\sin\gamma = \left[(1-p)\tilde{r}_0 - \frac{3(\rho_{\mathrm{el}} s_1)^2}{4\varepsilon_0 \varepsilon_{\mathrm{oil}} \tilde{b}_1^4 a\sigma} (1 + n\frac{\tilde{h}}{\tilde{b}_1})^{-4} \right] \sin\gamma \tag{A.18}$$

2. Computational procedure for the bridge profile

In this case, our goal is to compute the function $\tilde{z} = \tilde{z}(\tilde{r})$ for a capillary bridge that connects two spherical particles of radius *a*, separated at a surface-to-surface distance *h*. The input parameters are $\tilde{r}_{\mathrm{c}}, \tilde{h}$ and α. The steps of the computational procedure are as follows:

1) From Eq. (A.13), we calculate φ_{c}, $\tilde{z}_{\mathrm{c}}$ and θ_{c}.

2) We give a tentative value to $\tilde{r}_0$ to start a procedure for determining $\tilde{r}_0$ by the bisection method.

3) From Eqs. (A.4) and (A.6), we determine *p* and x_{c}.

4) With the value of $\tilde{z}_{\mathrm{c}}$ from point 1, we determine $\tilde{r}_0$ by solving Eq. (A.7) numerically using the bisection method. The integral in Eq. (A.7) is calculated numerically using the Simpson method.

5) With the determined value of $\tilde{r}_0$, the meniscus profile $\tilde{z} = \tilde{z}(\tilde{r})$ is computed from Eq. (A.3), using the Simpson method to calculate the integral numerically.

3. Computational procedure for $f_{\mathrm{cap}}(\gamma)$, $f_{\mathrm{sh}}(\gamma)$ and $f_{\max}$

To calculate $f_{\mathrm{cap}}(\gamma)$, the input parameters are $\tilde{h}, \Phi$ and α. The steps of the computational procedure are as follows:

1) We give a tentative value to $\tilde{r}_{\mathrm{c}}$ to start a procedure for determining $\tilde{r}_{\mathrm{c}}$ by the bisection method.

2) From Eq. (A.13), we calculate φ_{c}, $\tilde{z}_{\mathrm{c}}$ and θ_{c}.

3) We give a tentative value to $\tilde{r}_0$ to start a procedure for determining $\tilde{r}_0$ by the bisection method.

4) From Eqs. (A.4) and (A.6), we determine *p* and x_{c}.

5) With the value of $\tilde{z}_c$ from point 1, we determine $\tilde{r}_0$ by solving Eq. (A.7) numerically using the bisection method. The integral in Eq. (A.7) is calculated numerically using the Simpson method.

6) With the determined value of $\tilde{r}_0$, we calculate $\tilde{V}_c$ from Eq. (A.10).

7) For each given Φ, we determine $\tilde{r}_c$ by solving Eq. (A.15) numerically using the bisection method.

8) The dimensionless capillary force f_{cap} is calculated from Eq. (A.5).

9) The shearing angle γ and the dimensionless shear-response force f_{sh} are calculated from Eqs. (A.17) and (A.18). For this goal, we need also the values of additional parameters that enter Eq. (A.18), viz. ε_0, ε_{oil}, a, σ, $\tilde{b}_1$, ($\rho_{el}s_1$), and n.

10) f_{max} is determined as the maximal value of f_{sh}.

Appendix B. Additional experimental and computational results

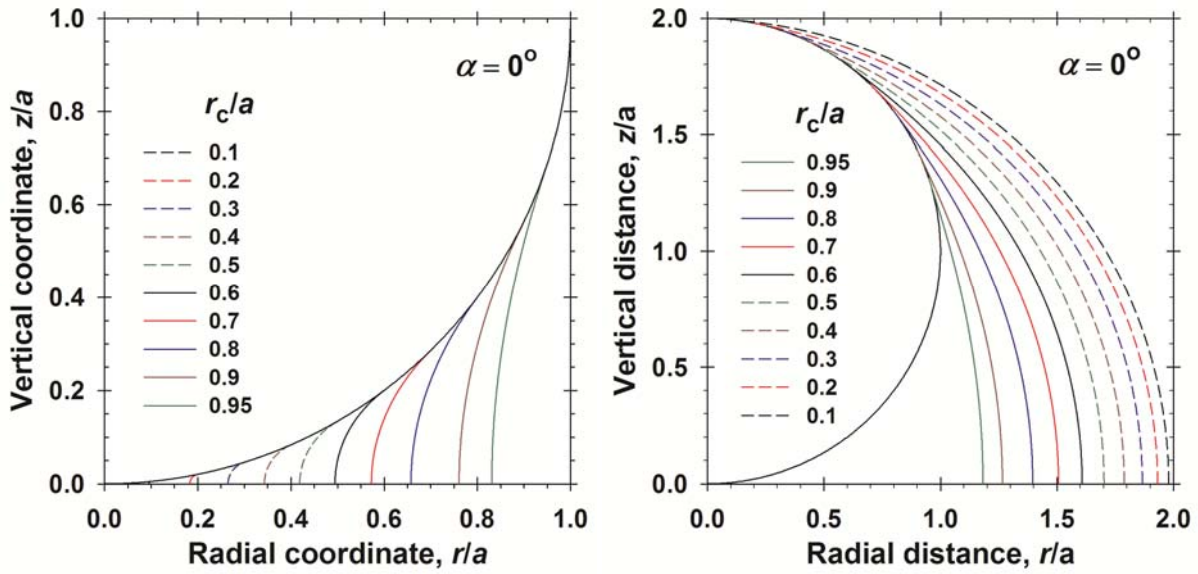

Fig. S1. Calculated profiles of capillary bridges, $z(r)$, for increasing bridge volume; the contact angle is fixed, α = 0º, whereas the position of the contact line, characterized by its radius, r_c, varies; r and z are cylindrical coordinates; the bridge connects two identical spherical particles of radius a, which are in a contact, h = 0. All profiles do not possess inflection points. For all of them, the capillary-bridge force, F_{cap}, is attractive.

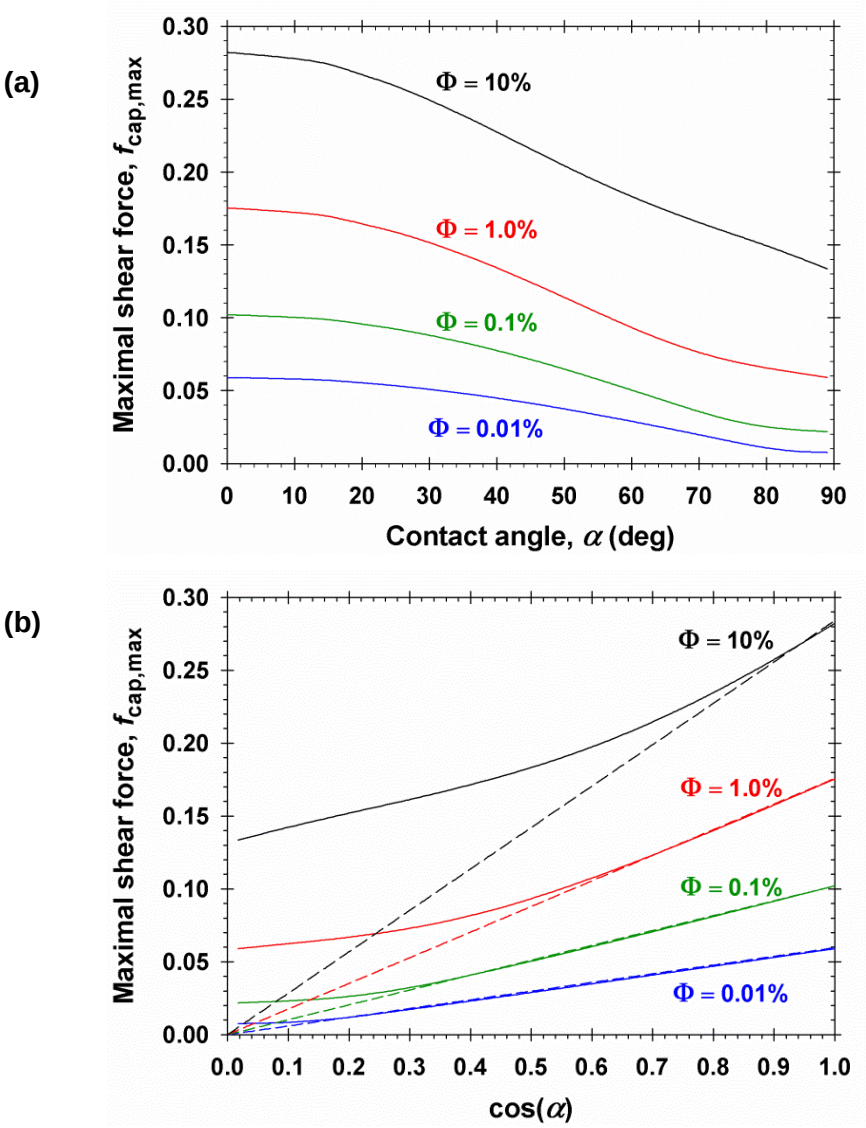

Fig. S2. Plots of the computed maximal projection of the dimensionless capillary-bridge force on the shear plane, $f_{cap,max}(\Phi,\alpha)$, (a) versus the contact angle α and (b) versus $\cos\alpha$, for various values of the dimensionless bridge volume, Φ. Here, $f_{cap,max}$ does not contain contribution from the electrostatic interparticle repulsion.

In the regions where the solid lines can be approximated with the dashed straight lines in Fig. S2, $f_{cap,max}(\Phi,\alpha)$ can be estimated from the formula (accuracy better than 0.6%) [27]:

$$f_{cap,max}(\Phi,\alpha) \approx (0.1763 + 0.0912\varphi + 0.0165\varphi^2)\cos\alpha \quad \text{for } \alpha \le \alpha_0$$
$$\alpha_0(\text{deg}) = 51.5 - 19.5\varphi - 2.5\varphi^2, \quad \varphi = \log_{10}\Phi(\%) \qquad \text{(B.1)}$$

$0.01\% \le \Phi \le 10\%$, where $\Phi = (1-\phi_p)S_i/(11.67\phi_p^2)\times 100\%$ and $S_i = \phi_i/(\phi_w + \phi_{oil})$, i = w, oil. $f_{cap,max}(\Phi,\alpha)$ given by Eq. (B.1) contains a contribution only from the capillary-bridge force, but does not contain contribution from the electrostatic interparticle repulsion, if any.

(a)

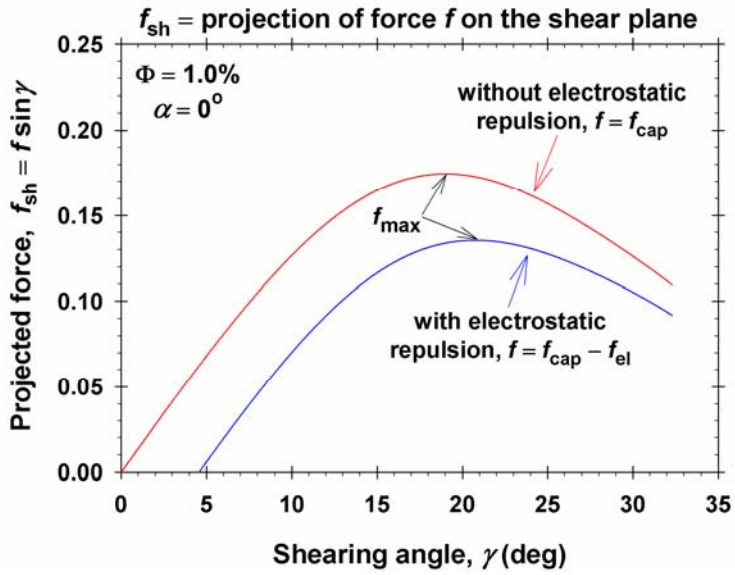

(b)

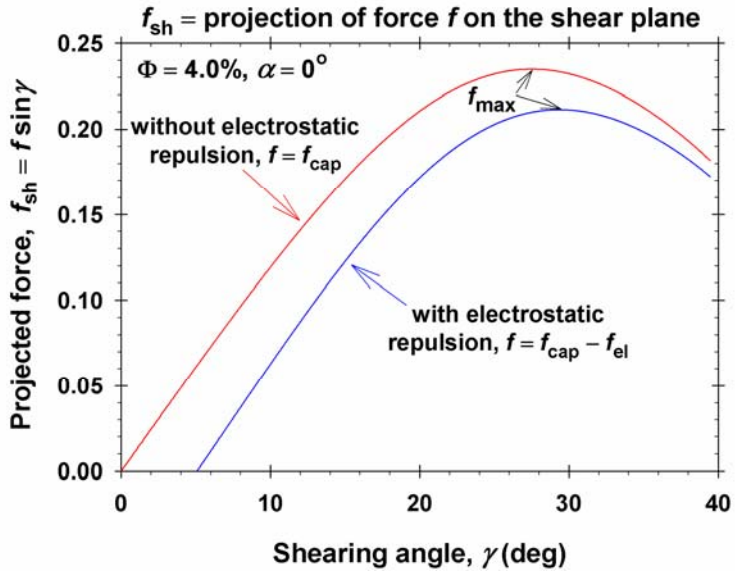

Fig. S3. Comparison of plots of the shear-response force, f_{sh}, vs. γ without and with electrostatic repulsion for $\alpha = 0^o$ and for (a) $\Phi = 1$ % and (b) $\Phi = 4$ %. The other parameter values (n, ε_{oil}, σ and a) correspond to Fig. 3c in the main text; $\widetilde{b}_1$ and ($\rho_{el}s_1$) are given by Eq. (24) therein. The graph illustrates that with the increase of the bridge volume Φ, the contribution of the electrostatic force (relative to the contribution of the capillary-bridge force) decreases.

Fig. S4 illustrates the fact that if the two capillary bridges do not overlap, the following relationship is satisfied:

$$\gamma + \varphi_c(h) + \varphi_c(0) < \frac{\pi}{2} \tag{B.2}$$

which is Eq. (26) in the main text.

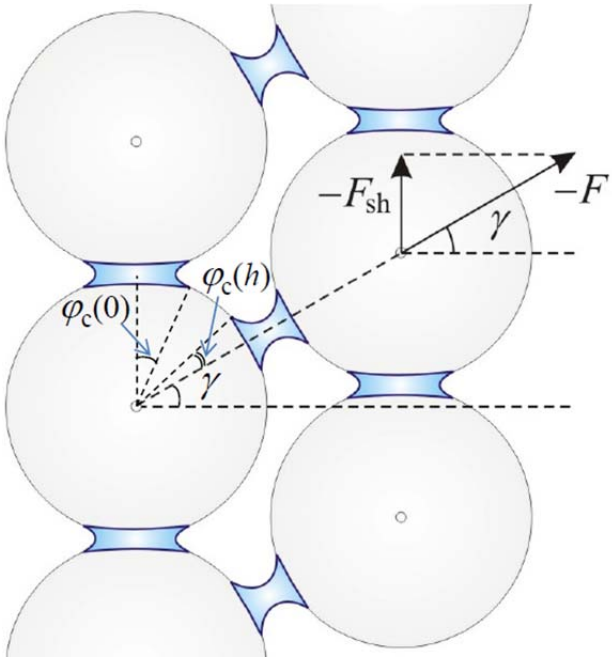

Fig. S4. Illustration of the fact that if $\gamma + \varphi_c(h) + \varphi_c(0) < \pi/2$, the two capillary bridges do not overlap.

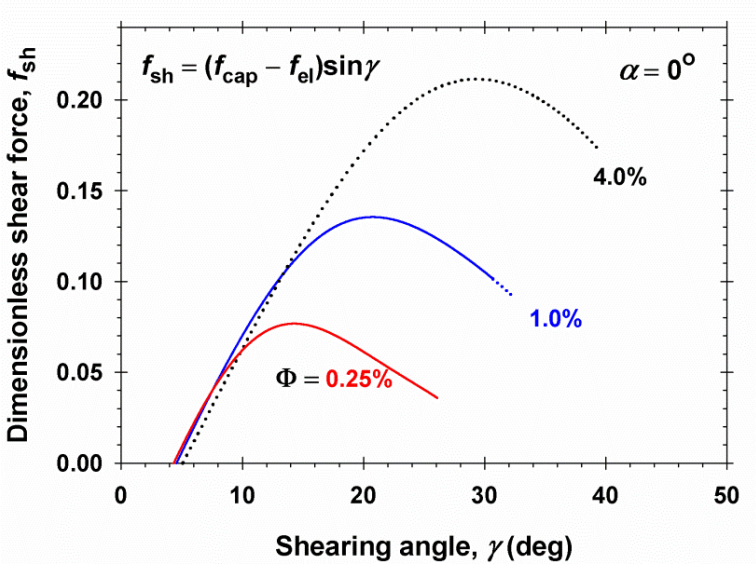

Fig. S5. Dependence of the dimensionless shear-response force, f_{sh}, on the shearing angle, γ, for contact angle $\alpha = 0^o$ and for three different values of the dimensionless bridge volume, Φ; the other parameter values (n, ε_{oil}, σ and a) correspond to Fig. 3c in the main text; $\tilde{b}_1$ and ($\rho_{el}s_1$) are given by Eq. (24) therein; six bridges per particle have been assumed. The dotted lines correspond to overlapping of capillary bridges, for which Eq. (B.2) is violated. For Φ = 0.25% all equilibrium capillary bridges are not overlapping. For Φ = 1 %, bridge overlapping could happen only at the greatest γ values, which are to the right of the maximum and do not affect the yields stress, Y. For Φ = 4 %, the bridges overlap for all values of γ.